geosciences

*Article*

# Early Evolution of the Adelaide Superbasin

**Jarred C. Lloyd [1,2,*], Alan S. Collins [1], Morgan L. Blades [1], Sarah E. Gilbert [3] and Kathryn J. Amos [2]**

[1] Tectonics and Earth Systems Group and Mineral Exploration CRC, Department of Earth Sciences, University of Adelaide, Adelaide, SA 5005, Australia; alan.collins@adelaide.edu.au (A.S.C.); morgan.blades@adelaide.edu.au (M.L.B.)
[2] Australian School of Petroleum and Energy Resources, University of Adelaide, Adelaide, SA 5005, Australia; kathryn.amos@adelaide.edu.au
[3] Adelaide Microscopy, University of Adelaide, Adelaide, SA 5005, Australia; sarah.gilbert@adelaide.edu.au
* Correspondence: jarred.lloyd@adelaide.edu.au

**Abstract:** Continental rifts have a significant role in supercontinent breakup and the development of sedimentary basins. The Australian Adelaide Superbasin is one of the largest and best-preserved rift systems that initiated during the breakup of Rodinia, yet substantial challenges still hinder our understanding of its early evolution and place within the Rodinian supercontinent. In the past decade, our understanding of rift and passive margin development, mantle plumes and their role in tectonics, geodynamics of supercontinent breakup, and sequence stratigraphy in tectonic settings has advanced significantly. However, literature on the early evolution of the Adelaide Superbasin has not been updated to reflect these advancements. Using new detrital zircon age data for provenance, combined with existing literature, we examine the earliest tectonic evolution of the Adelaide Superbasin in the context of our modern understanding of rift system development. A new maximum depositional age of 893 ± 9 Ma from the lowermost stratigraphic unit provides a revised limit on the initiation of sedimentation and rifting within the basin. Our model suggests that the basin evolved through an initial pulse of extension exploiting pre-existing crustal weakness to form half-grabens. Tectonic quiescence and stable subsidence followed, with deposition of a sourceward-shifting facies tract. Emplacement and extrusion of the Willouran Large Igneous Province occurred at c. 830 Ma, initiating a new phase of rifting. This rift renewal led to widespread extension and subsidence with the deposition of the Curdimurka Subgroup, which constitutes the main cyclic rift sequence in the Adelaide Superbasin. Our model suggests that the Adelaide Superbasin formed through rift propagation to an apparent triple junction, rather than apical extension outward from this point. In addition, we provide evidence suggesting a late Mesoproterozoic zircon source to the east of the basin, and show that the lowermost stratigraphy of the Centralian Superbasin, which is thought to be deposited coevally, had different primary detrital sources.

**Keywords:** Adelaide Superbasin; Neoproterozoic; detrital zircon; geochronology; provenance; rift basin

**Citation:** Lloyd, J.C.; Collins, A.S.; Blades, M.L.; Gilbert, S.E.; Amos, K.J. Early Evolution of the Adelaide Superbasin. *Geosciences* **2022**, *12*, 154. https://doi.org/10.3390/geosciences12040154

Academic Editors: Andrew C. Morton, Shane Tyrrell and Gustavo Zvirtes

Received: 17 February 2022
Accepted: 26 March 2022
Published: 29 March 2022

## 1. Introduction

The breakup of the supercontinent Rodinia, and subsequent formation of Gondwana, coincided with critical Earth system changes that led to the Phanerozoic world of extensive macroscopic mineralised life, significantly oxygenated atmosphere and hydrosphere, and a buffered climate devoid of whole-planet glaciations [1–3]. Determining any interdependence between these phenomena, e.g., [1,4–6], requires constructing full-plate tectonic reconstructions of the globe [7,8], which necessitate a fundamental understanding of the temporal link between tectonically controlled geological features (such as rift basins) and plate tectonic phenomena (such as continental plate sundering and ocean crust formation [8,9]).

The Adelaide Superbasin [10] is one of the largest and best-preserved rift to passive-margin successions to form during the Neoproterozoic breakup of Rodinia, which included large continental rifts between the Australia, Amazonia, Baltica, Kalahari, Laurentia, and Siberia cratons [11–13]. The Adelaide Superbasin is thought to have formed the conjugate margin to western Laurentia in Rodinia [8,14–19], although other configurations for Rodinia have been suggested, e.g., [13,20–22]. Poor chronological control, sparse and ambiguous palaeomagnetic constraints, and a lack of young detrital zircon in the lower units of the Adelaide Superbasin have long hindered the research and testing of these Rodinia reconstructions. Research on the tectonic evolution of the Adelaide Superbasin has seen the geosyncline theory [23] and transition to plate tectonics [24,25], with a few targeted [26–28] or more generalized [10,29] studies since.

This research presents new detrital zircon U–Pb and trace element data for the lowermost units of the Adelaide Rift Complex within the Adelaide Superbasin. We use these data, together with existing literature, to provide a refined, early tectonic evolution of the rift system during the deposition of the Callanna Group.

## 2. Geological Background

### 2.1. Adelaide Superbasin

The Adelaide Superbasin [10] is a large, Neoproterozoic to middle Cambrian sedimentary system at the southeast margin of Proterozoic Australia which formed as a result of the breakup of the supercontinent Rodinia. The Adelaide Superbasin consists of several named basins and sub-basins that span from the Neoproterozoic to early Cambrian. The largest and oldest of these is the Adelaide Rift Complex, which is contiguous with the relatively undeformed rocks of the Torrens Hinge Zone, Stuart Shelf [23], and Coombalarnie Platform [30]. Two Cambrian basins, the Arrowie Basin and Stansbury Basin, are also considered part of the Adelaide Superbasin [10,31] (Figure 1). Whereas present-day exposure of the sedimentary basin is approximately 600 km from north to south, the basin spans over 1100 km from central Australia to Kangaroo Island. Deposition within the Adelaide Superbasin spans over 300 million years of Earth's history and stretches from the northernmost regions of South Australia, narrowing in the South Mount Lofty Ranges at the Fleurieu Peninsula and extending onto Kangaroo Island. Further south, links with coeval sequences in Antarctica and eastern Tasmania are unclear, but possible [32]. The Archaean to Mesoproterozoic Gawler Craton lies to the west of the Adelaide Superbasin, and the late Palaeoproterozoic to early Mesoproterozoic Curnamona Province lies to the east. Laurentia is thought to have lain to the east/southeast of the Adelaide Superbasin within Rodinia, and East Antarctica is understood to have been joined to the south of the Gawler Craton as the Mawson Continent (e.g., [10] and references therein). The Adelaide Superbasin began as an intracontinental rift system that successfully progressed to a passive margin basin in its southeast region yet remained a failed rift in the north. Deposition within the basin ceased during the Delamerian orogeny c. 514–490 Ma [25,33–35].

The stratigraphy of the Adelaide Superbasin is divided into three supergroups [25], two for the Neoproterozoic sequences and the third for the Cambrian sequences, with numerous group- and subgroup-level divisions. In the Neoproterozoic, the Warrina Supergroup is comprised of the Callanna, Burra, and Poolamacca Groups, and the Heysen Supergroup contains the Umberatana, Wilpena, Torrowangee, and Farnell Groups. Each of these groups are further divided into numerous subgroups, as described by the authors of [10]. The Warrina Supergroup encompasses the Tonian early rift sequences that are largely restricted to fault-bound depositional troughs, and the Heysen Supergroup is comprised of the Cryogenian and Ediacaran glacial, interglacial, and postglacial sedimentary rocks, with a greater area of deposition within a passive margin setting. The timing of rift termination is not well established. However, evidence of large-scale normal faulting is not seen after the early Cryogenian [25]. Here, we focus on the Callanna Group, which is best preserved in the failed arm of the rift system. The reader is referred to Preiss [24], Preiss [25], Counts [36], Lloyd et al. [10], Cowley [37], and references therein for further detail on the geological history of the Adelaide Superbasin.

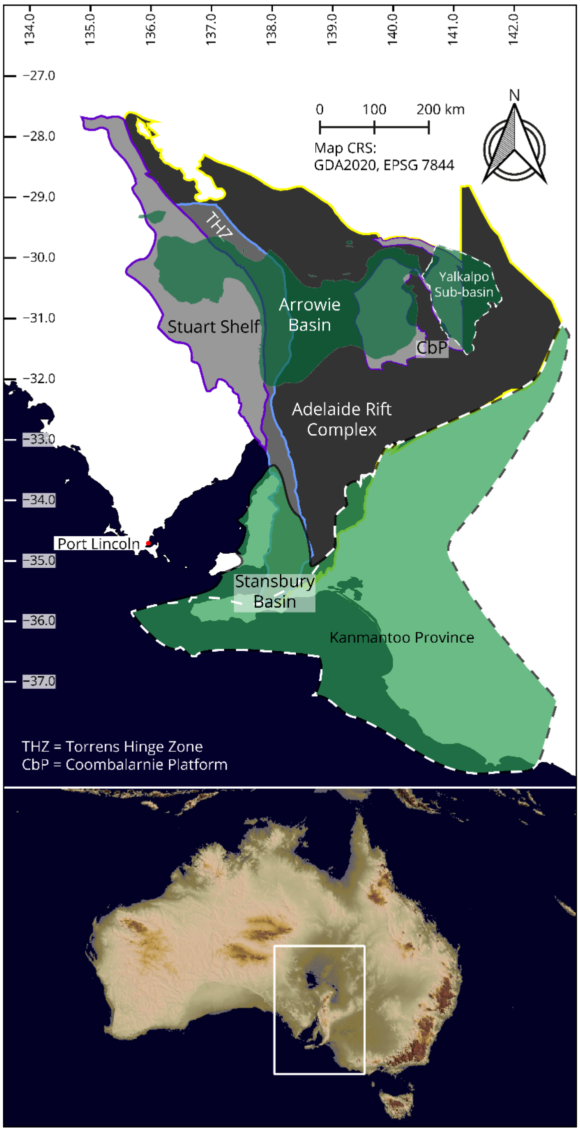

**Figure 1.** Map of the known Adelaide Superbasin extent and basin subdivisions, derived from [10].

### 2.2. Callanna Group

The oldest stratigraphy of the Adelaide Superbasin is represented by the Callanna Group [38], which is further subdivided into the Arkaroola Subgroup [38–40] and the Curdimurka Subgroup [38], with the latter inferred to be the younger of the two [41]. For historical reference, the now-outdated "Willouran Series" is equivalent to the Callanna Group, although this has not always been the case [24]. In New South Wales, the Poolamacca Group [42] is thought to be the equivalent of the Arkaroola Subgroup [24]. The known depositional extent of the Callanna Group (Figure 2) is restricted to the eastern (NSW), central, and northern Adelaide Rift Complex (including the Davenport and Denison Ranges), Stuart Shelf, and possibly the eastern Officer Basin.

The Callanna Group is characterised by initially siliciclastic sedimentation transitioning to carbonate and evaporite dominated deposition, with minor, interbedded, mafic to intermediate volcanic and volcanogenic sequences. The Arkaroola Subgroup (Figure 3, Supplementary Figure S1) comprises basal siliciclastic units (e.g., Younghusband Conglomerate, Paralana Quartzite), overlain by a (meta-)carbonate unit (e.g., Wywyana Formation), and finally capped by mafic (meta-)igneous rocks (e.g., Wooltana Volcanics). The basal siliciclastic and middle carbonate sequences are thought to have been deposited in sag basins from the gradual subsidence of a stable craton prior to rifting [25]. Alternately, these sequences may have been deposited as syn-rift sediments penecontemporaneous with faulting [43]. The igneous sequences at the top of the Arkaroola Subgroup are almost exclusively metabasaltic rocks with minor interbedded sediments [24,44]. These igneous sequences are inferred to have been extruded in subaerial settings [44] as continental tholeiitic (flood) basalts [24,25,44–47]. The Wooltana Volcanics and its equivalent units of the uppermost Arkaroola Subgroup are the most voluminous igneous rocks recognised in the Adelaide Superbasin and have been termed the "Willouran Large Igneous Province (LIP)", "Willouran Basic Province", or "Gairdner LIP" [44,45,47–51]. Neoproterozoic mafic volcanics of the Coompana Province c. 860 Ma may also be part of the Willouran LIP [52]. The Willouran LIP (Figure 2) is interpreted to represent the first major phase of rifting within the Adelaide Superbasin, and thus the initiation of Rodinia breakup at the eastern margin of Proterozoic Australia that led to the development of the proto-Pacific Ocean [8]. Presently, the only exposures of complete sections of the Arkaroola Subgroup (Figure 3) are located in the Arkaroola/Mount Painter area, and the Davenport and Denison Ranges (Peake and Denison Inliers) (Supplementary Figure S1). Isolated blocks of the Arkaroola Subgroup are recognised in carbonate megabreccia (diapirs) throughout the Adelaide Superbasin, particularly within the Willouran Ranges. The equivalent Poolamacca Group crops out in the Barrier Ranges of New South Wales (Figure 1).

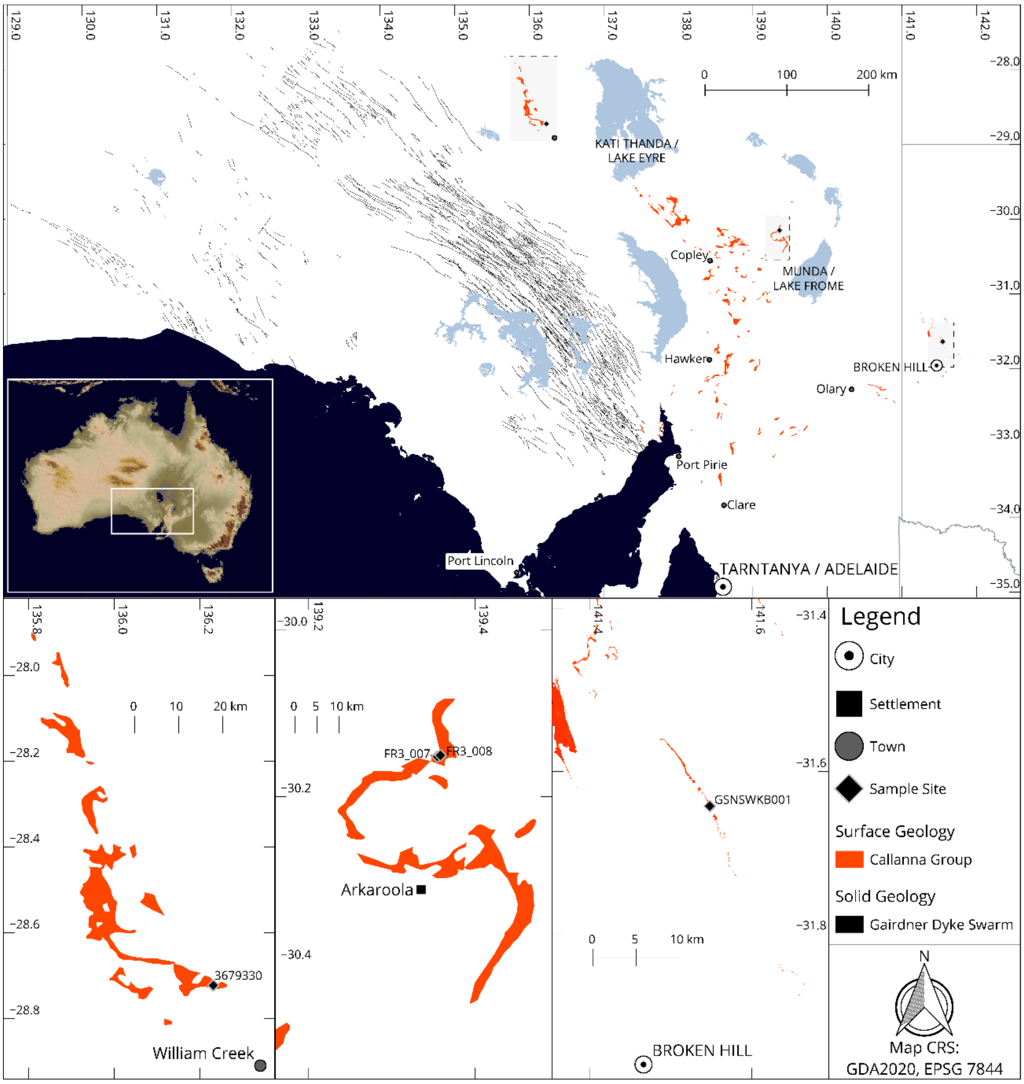

**Figure 2.** Distribution of the exposed Callanna Group rocks (orange), the subsurface distribution of the Gairdner Dolerite (black lines), and insets showing sample locations (west to east).

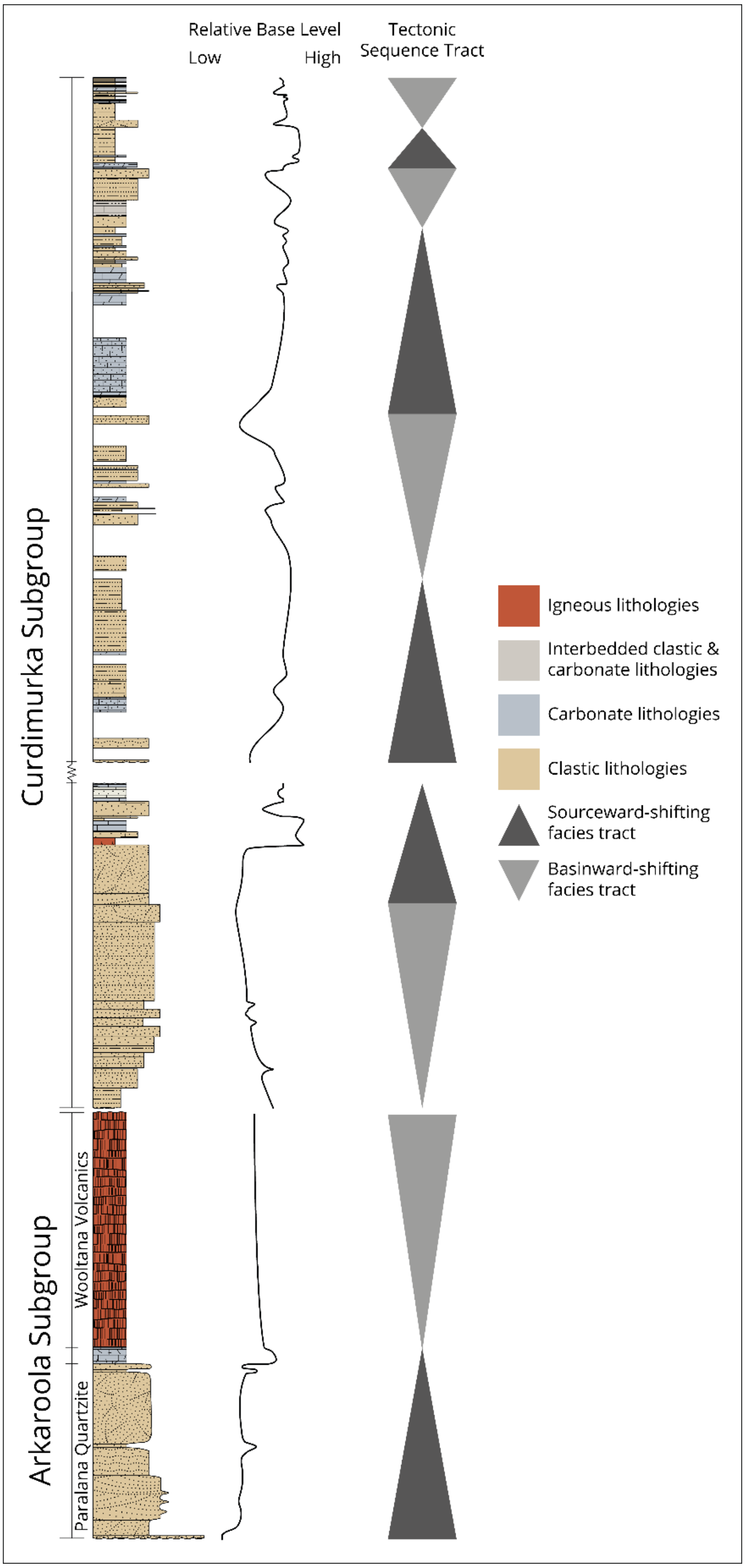

**Figure 3.** Simplified (composite) stratigraphic log of the Callanna Group based on the type sections from Arkaroola and the Willouran Ranges. This shows the generalised stratigraphy representative of the Callanna Group across the Adelaide Superbasin. Relative base level utilises further information from Mackay [27] and Preiss [24,25]. Tectonic successions follow the terminology of Matenco and Haq [53].

Sourceward-shifting facies tracts are where accommodation space was created faster than the rate of sediment supply ($\delta AS/SS \geq 1$), and basinward-shifting facies tracts are where the rate of sediment supply was faster than the creation of accommodation space ($\delta AS/SS \leq 1$). For detailed lithology patterns and additional stratigraphic unit names, see Supplementary Figure S1.

The Curdimurka Subgroup is thought to overlie the Arkaroola Subgroup and locally exceeds 8 km stratigraphic thickness. As a result of tectonic and salt tectonic dismemberment, no wholly intact section through the Curdimurka Subgroup has been identified [24,25,27,38,54–56]. However, composite sections have been developed for the Willouran Ranges [38] (Figure 3), the Davenport and Denison Ranges [54], the Worumba Anticline [56], and the Spalding Inlier [57]. The most intact of these composite sections is within the Willouran Ranges (Supplementary Figure S1). The Curdimurka Subgroup is comprised of a cyclical sequence of evaporitic mixed carbonate and siliciclastic rocks, with minor intermediate to felsic igneous rocks [24,25,27,54,58,59]. The carbonate sequences comprise stromatolitic limestones and dolostones, and cryptalgal dolostone with abundant evaporite mineral pseudomorphs and local tepee structures. The siliciclastic sequences include laminated, pyritic, and carbonaceous siltstone, and sandstones and siltstones with occasional graded bedding, halite casts, and load casts. In addition, feldspathic- and carbonate-cemented cross-bedded sandstone, with occasional heavy mineral laminations and halite casts, are present. The stratigraphic names of the Callanna Group, general geographic locations, and approximate relative stratigraphic positions (correlations) are outlined in Supplementary Figure S1. Supplementary Figure S1 also highlights the significant thickness variations of coeval sequences across the Adelaide Superbasin. Within a given region, significant tectonically controlled local thickness variations occur (e.g., Paralana Quartzite changes thickness by approximately 700 m across the Paralana Fault).

## 3. Materials and Methods

Three samples were analysed for detrital zircon geochronology, two from the Paralana Quartzite (FR3_007, FR3_008; Figure 2) and one from the Lady Don Quartzite in the eastern part of the superbasin (GSNSWKB001; see Figure 2). The two Paralana Quartzite samples were obtained near the western flank of the Mawson Plateau in the Arkaroola Wilderness Sanctuary, one from the basal member, and one from the top of the same stratigraphic sequence. A fourth volcano-sedimentary sample, 3679330, from the Davenport and Denison Ranges in the far northwest of the superbasin (Figure 2), was also analysed in the hope of obtaining an indication of the crystallisation age of the Cadlareena Volcanics—a presumed equivalent of the Wooltana Volcanics [54]. These samples were selected to investigate the provenance of earliest sedimentary rocks of the Adelaide Superbasin and any spatially related variations in coeval sequences.

Rock samples were first prepared for detrital zircon analysis by crushing the rock samples using a jaw crusher and disk mill. Then, the samples were sieved using nylon mesh of 79 μm and 400 μm. All equipment was thoroughly cleaned by vacuuming, ethanol, and compressed air between each sample. New sieve mesh was used for each sample. Mineral separation was completed by water panning the 79–400 μm fraction and using LST heavy liquid set to a density of $2.85 \pm 0.02$ g cm$^{-3}$. Zircon was then handpicked and mounted in an epoxy resin. Any grain that remotely resembled a zircon was picked to minimise human bias, an issue highlighted by Sláma and Košler [60] and Dröllner et al. [61]. Where permitted by zircon yields, at least 300 zircons were picked per sample. Otherwise, all zircons in the sample were picked. The mounts were then imaged via cathodoluminescence on either an FEI Quanta 600 scanning electron microscope (for zircon analysed in 2020) or a Cameca SXFive Electron Microprobe (for zircon analysed in 2021). The zircons were then analysed using Laser Ablation Inductively Coupled Plasma Mass Spectrometry (LA-ICP-MS) to obtain a suite of elemental data for U–Pb geochronology and rare earth element (REE) analysis. All zircons were analysed using a Resonetics M-50

(193 nm ArF excimer) laser ablation system coupled with an Agilent 7900x inductively coupled plasma mass spectrometer. All analytical instruments used are housed at Adelaide Microscopy, University of Adelaide, Australia.

Four standards were used during analysis: GEMOC GJ-1 [62,63], Plešovice [63,64], 91500 [63,65,66], and NIST610 glass [67]. Unknowns were bracketed by two analyses of GJ-1, followed by a combined two to three analyses of Plešovice and 91500, and two analyses of NIST610 for every 20–30 unknowns. GJ-1 was used as the primary calibration standard for U–Pb ratios, and NIST610 was used as the primary calibration standard for Pb isotope ratios and trace element data (See more in Appendix A). Zirconium-91 was used as the internal standard for trace element data with a value of 431,400 ppm (43.14 wt%) $^{91}$Zr assigned to unknowns. Plešovice and 91500 were used as validation standards. A 30 s gas blank, followed by either a 40 s or 30 s ablation (session on 30 March 2021) time, was used with a laser repetition rate of 5 Hz. A spot size of 29 µm and a nominal fluence of 2 J cm$^{-2}$ was used for zircon, and a spot size of 43 µm using a nominal fluence of 3.5 J cm$^{-2}$ was used for NIST610. Data were processed using LADR [68], version 1.1.06, and output as "Full Analytical Uncertainty". No common Pb corrections were applied to the data. Reference material ratios for GJ-1, Plešovice, and 91500 were set to the Chemical Abrasion Isotope Dilution Thermal Ionisation Mass Spectrometry (CA-ID-TIMS) values (uncorrected for thorium disequilibria and common-Pb) of Horstwood et al. [63]. Weighted averages and dispersion statistics for all standards are available from the link in "Data Availability".

Statistical analysis of the zircon U–Pb data followed the method of Lloyd et al. [10]. Data were considered concordant if they were within ± 10%, and a "meaningful" age if the 2σ uncertainty was ≤10%. If a datum satisfied both parameters, it was termed a "Filtered Age". Maximum depositional ages were determined from a stricter 2% concordance filter, and we used the older age of the three isotope ratios ($^{207}$Pb/$^{235}$U, $^{206}$Pb/$^{238}$U, $^{207}$Pb/$^{206}$Pb) for a conservative estimate of the youngest single concordant grain. All ages were quoted with 2σ uncertainty. Kernel density estimates (KDEs), and multidimensional scaling plots (MDS) were generated using IsoplotR [69]. Key zircon trace element data are presented graphically using methods following Verdel et al. [70]. In addition, lanthanoid data are represented using violin plots and lambda representation [71,72].

Metadata for the LA-ICP-MS sessions, data for all analyses, cathodoluminescence images, and R code used to generate plots are available from the links in "Data Availability".

## 4. Results

A total of 161 analyses were conducted for sample FR3_008. Of these, 141 analyses passed filtering parameters, with ages ranging from 2914 ± 46 Ma to 892 ± 13 Ma (Figure 4). The primary population peak of this sample was c. 1550 Ma, with a secondary peak c. 1750 Ma, and tertiary peaks c. 1180 Ma and 935 Ma. Four analyses were outside these populations, ranging from 2914 ± 46 Ma to 2237 ± 57 Ma. Notably, a small cluster of zircons occurred c. 900 Ma.

A total of 125 analyses were conducted for sample FR3_007. Of these, 99 analyses passed filtering parameters, with ages ranging from 3090 ± 31 Ma to 1305 ± 17 Ma (Figure 4). The primary population peak of this sample was c. 1680 Ma, with secondary population peaks c. 2480 Ma, 2000 Ma, and 1480 Ma. Three analyses were outside these populations, ranging from 3097 ± 27 Ma to 2819 ± 60 Ma.

A total of 114 analyses were conducted for sample GSNSWKB001. Of these, 85 analyses passed filtering parameters, with ages ranging between 3090 ± 31 Ma and 1302 ± 23 Ma (Figure 4). The primary population peak of this sample was c. 1620 Ma, with a secondary peak c. 1840 Ma. These two peaks formed a bimodal population ranging from 1999 ± 32 Ma to 1302 ± 23 Ma.

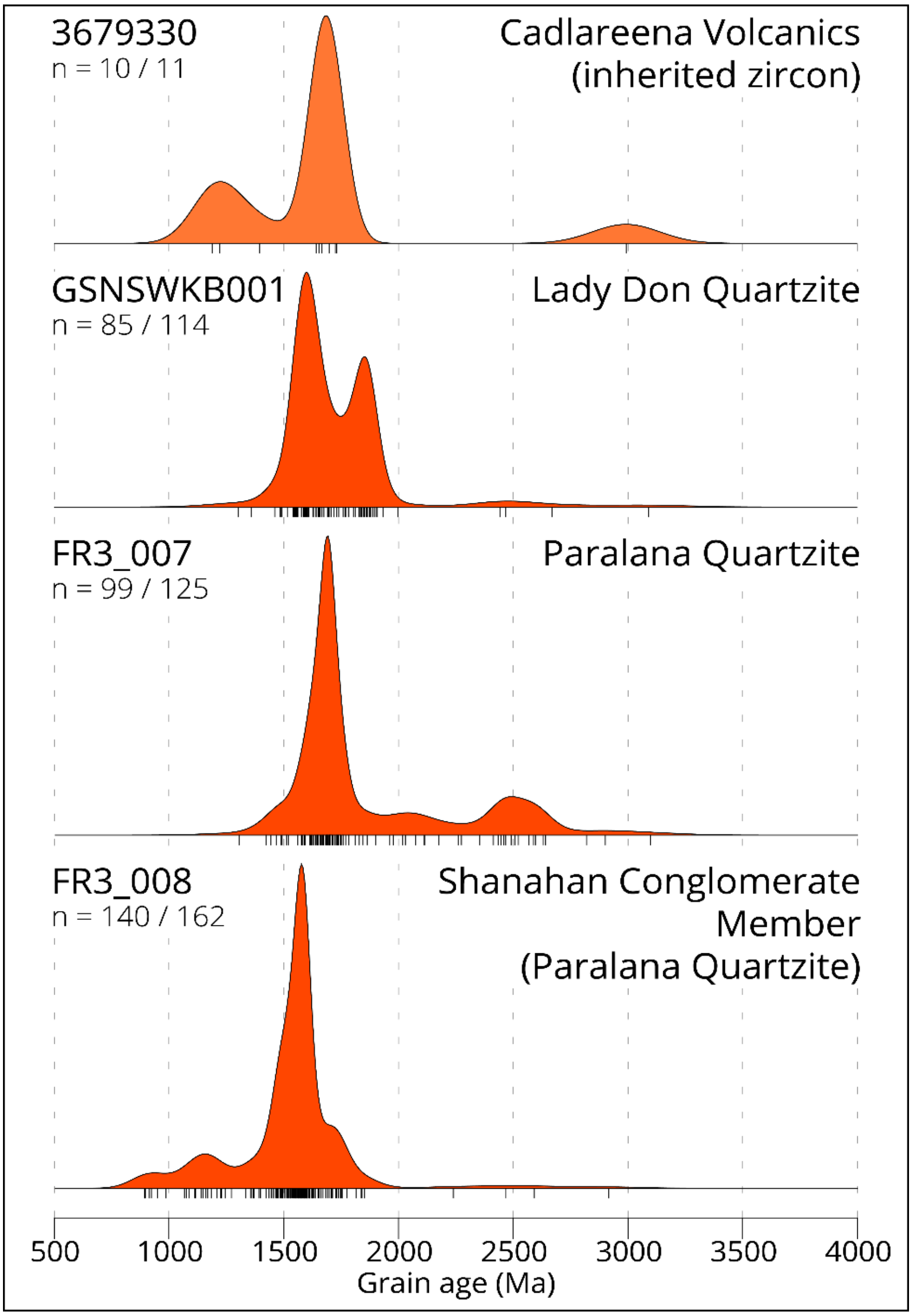

**Figure 4.** Kernel density estimate plots of the four samples analysed in this study. The plots are shown in ascending stratigraphic order. Tick marks below each plot represent an analysis. n = filtered analyses/total analyses. Created using IsoplotR [69].

From the small quantity of sample that was crushed for sample 3679330, 11 zircons were obtained and analysed, with 10 of these within filtering parameters. The oldest grain yielded an age of 2992 ± 27 Ma, the youngest grain was 1189 ± 18 Ma, and the remainder ranged between 1222 ± 22 Ma and 1725 ± 24 Ma, with a cluster of four grains c. 1680 Ma (Figure 4).

Lanthanoid concentrations are typical for zircons, with a several orders-of-magnitude increase in concentration from light to heavy elements, a slight negative deviation in europium (Eu), and a positive deviation in cerium (Ce) (Figure 5).

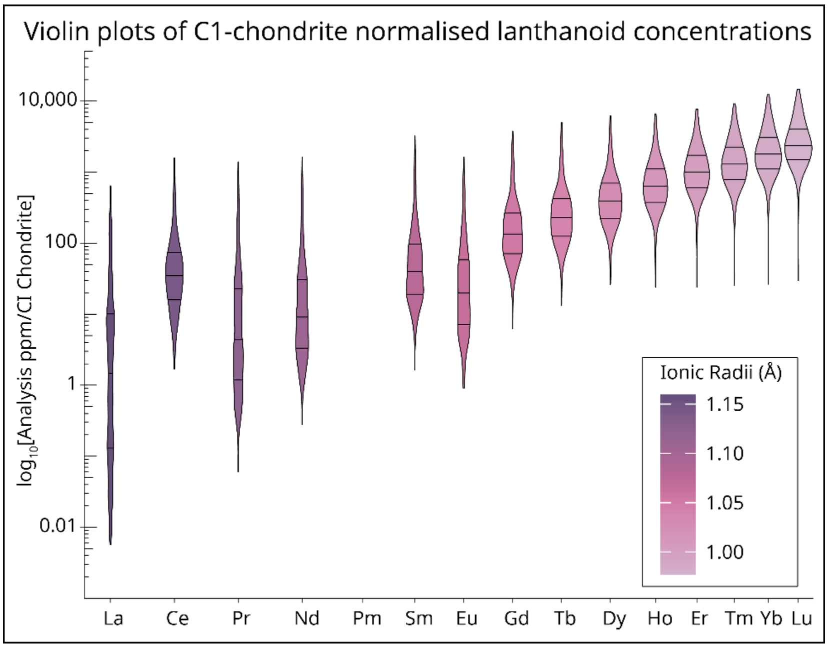

**Figure 5.** Violin plots of CI chondrite [72]-normalised lanthanoids for all filtered zircon analysed in this study. This plot shows the overall distribution by density estimation of lanthanoid concentrations in all filtered zircons presented in this study. The *X*-axis is spaced by ionic radii [73] and ordered by atomic number. Black lines across the fill of each plot represent the 0.25, 0.5, and 0.75 quantiles. Bandwidth of the density estimates was calculated using the Botev algorithm from the Provenance package [74].

## 5. Discussion

### *5.1. Provenance and Maximum Depositional Ages*

### 5.1.1. Paralana Quartzite, Including Shanahan Conglomerate Member

Samples FR3_007 and FR3_008 were both sampled from the Paralana Quartzite. However, FR3_008 was sampled from a stratigraphically lower position, mapped as the Shanahan Conglomerate Member. The MDA of the Paralana Quartzite combines the results of both samples.

The youngest zircon in FR3_008 (analysis FR3_008-090, Figure 6) originally yielded $^{207}$Pb/$^{235}$U, $^{206}$Pb/$^{238}$U, and $^{207}$Pb/$^{206}$Pb ages of 897 ± 46 Ma, 896 ± 18 Ma, and 889 ± 39 Ma, respectively. To verify the age obtained, this zircon was reanalysed on a subsequent analytical session with two additional analyses. The second analysis (FR3_008_run2-003, Figure 6) yielded $^{207}$Pb/$^{235}$U, $^{206}$Pb/$^{238}$U, and $^{207}$Pb/$^{206}$Pb ages of 893 ± 39 Ma, 892 ± 13 Ma, 886 ± 30 Ma, respectively. The third analysis (FR3_008_run2-004, Figure 6) yielded a younger discordant age, likely due to a small inclusion that can be seen in Figure 6.

The two concordant signals had Th/U ratios of ~0.55, and the discordant analysis had a Th/U ratio of ~1.3. A concordia age of 893 ± 9 Ma, MSWD 0.067, p($\chi$2) 0.98 was calculated from the two concordant analyses, and a traditional uncertainty weighted mean yielded a $^{206}$Pb/$^{238}$U age of 893 ± 10 Ma, MSWD 0.14 Ma, p($\chi$2) 0.71. Both calculations propagate external uncertainties [69]. The zircon was euhedral, with simple regular growth zoning presenting a {101} form [75,76]. Although one end of the zircon appeared to have broken off, the aspect ratio was at least 3.3:1. As the concordia age is the statistically "most likely" age [77,78], uses the most amount of available analytical data from the multiple analyses of the single grain, and is in good agreement with individual calculated decay ages and the $^{206}$Pb/$^{238}$U-weighted mean, it was used as the age of crystallisation and, subsequently, the maximum depositional age for the Paralana Quartzite. This revises the maximum depositional age of the Paralana Quartzite from 1177 ± 28 Ma [10] to 893 ± 9 Ma. There were three additional zircons with ages c. 980–900 Ma, two of which were long, euhedral zircons, and the third was a euhedral overgrowth. This suggests that the youngest zircon, 893 ± 9 Ma, was not a result of contamination.

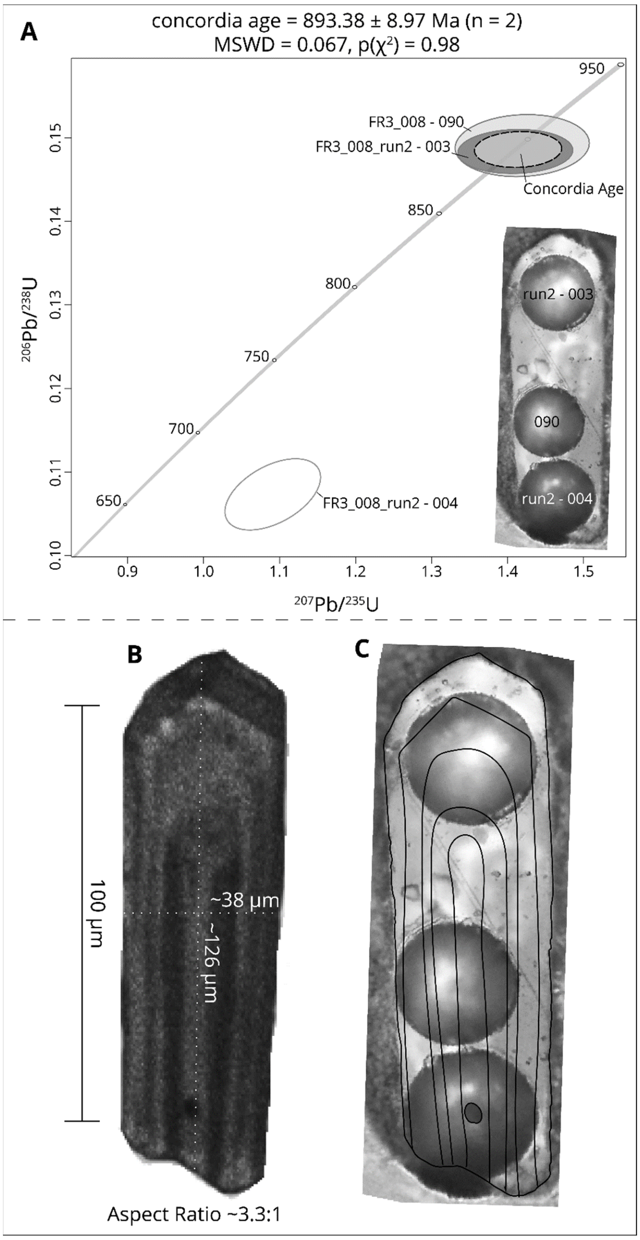

**Figure 6.** (**A**) Concordia plot and age of the three spots analysed on the youngest single zircon for FR3_008 (Shanahan Conglomerate Member). Spots are labelled on the reflected light image. (**B**) Cathodoluminescence image overlain with measurements for aspect ratio. (**C**) Outlines of growth zones and inclusion overlain on reflected light image. Concordia plot generated using IsoplotR [69].

Both samples, FR3_008 (Shanahan Conglomerate Member) and FR3_007 (Paralana Quartzite), had an overlapping population of zircons c. 1800–1300 Ma, with their primary population peaks centred c. 1580 Ma and c. 1690 Ma, respectively (Figure 4). These primary zircon populations were likely derived locally from the Ninnerie Supersuite and/or Radium Creek Group [79–82]. The two sample populations differed significantly with the direction of the population tails. Sample FR3_008 tailed toward younger ages, with an additional minor population peak c. 1150 Ma and small cluster of grains c. 900 Ma (Figure 4). There were only four zircons older than c. 1850 Ma present in sample FR3_008. In contrast, sample FR3_007 tailed toward older ages, with an additional minor population peak c. 2500 Ma (Figure 4) and no zircon younger than c. 1300 Ma. Zircons from the older tail of sample FR3_008, particularly the c. 2500 Ma population, were most likely derived from the Gawler Craton (Figure 7), namely the Mulgathing Complex and Sleaford Complex [83–85], as previously suggested [10]. The younger c. 1300–1050 Ma zircon population in sample FR3_008 was most likely derived from the Musgrave Province (Figure 7) [86–90]. However, they could have alternately been sourced from a yet-undiscovered but inferred Musgrave-like, late Mesoproterozoic (c. 1300–1000 Ma) source to the east [27,91–93]. The five youngest zircons present in sample FR3_008, younger than 1000 Ma, are enigmatic. They have no known local source terrane. Moreover, given the euhedral to subhedral nature of these grains and the breccia-conglomerate nature of the rock, it is unlikely they were transported a great distance. It is possible these zircons were derived from a yet-undiscovered or previously destroyed minor magmatic sequence that would mark initial volcanism of the Adelaide Superbasin that precedes flood basalt emplacement. The zircon populations and lithological differences between the two samples, which were sampled approximately 350 m from each other, suggest a change in the sediment source up stratigraphy to include a greater percentage of more distal source areas, and a loss of the younger source material.

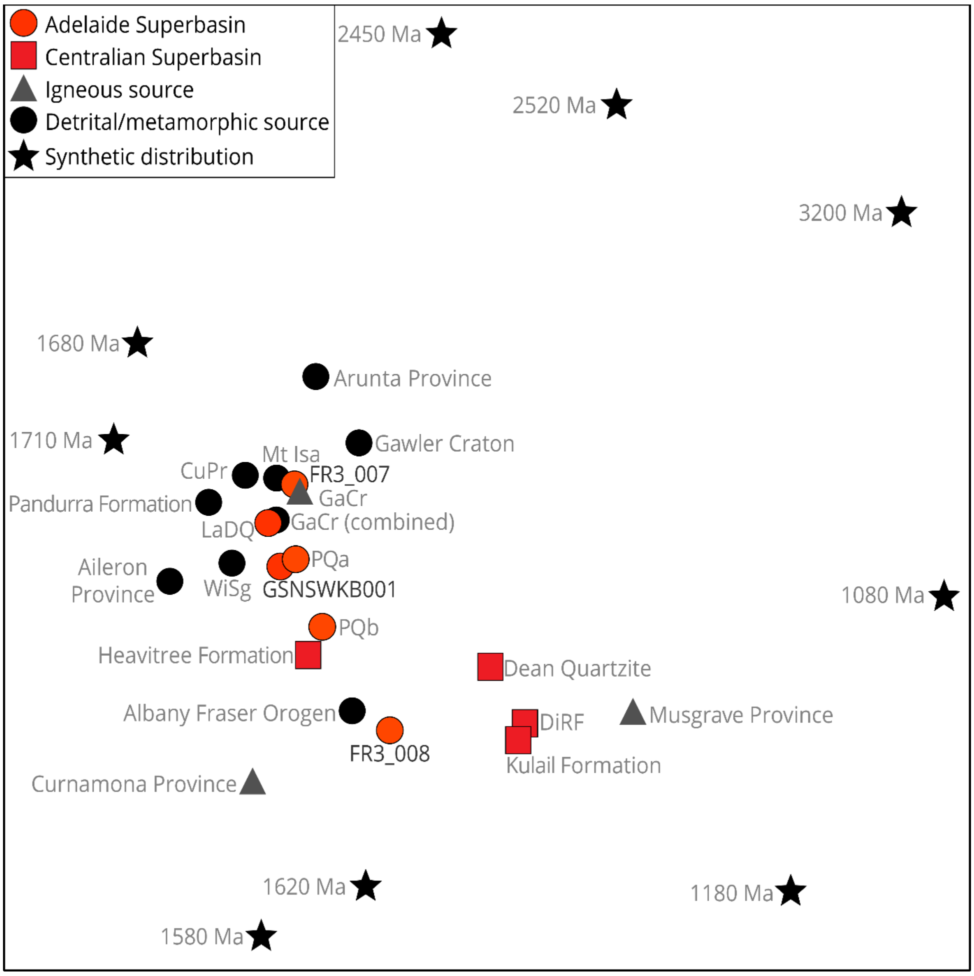

**Figure 7.** Non-metric multidimensional scaling plot of samples analysed (n > 40) in this study (orange circles) with data from potential correlative formations of the Centralian Superbasin (red squares), potential source regions (black and grey circles and triangles), and synthetic distributions of main population peaks and key zircon growth events in the region. This plot shows relative similarity of all data to each other and is intended as a visual guide. Points that plotted closer together suggest greater similarity. Axes were omitted, as the algorithm produced normalised values with no physical meaning which could be safely removed. Produced using IsoplotR [69]. Abbreviations: CuPr = Curnamona Province; GaCr = Gawler Craton (combined signifies detrital, metamorphic, and igneous data); WiSg = Willyama Supergroup, DiRF = Dixon Range Formation, PQ = Paralana Quartzite. Data were taken from this study and the existing literature (a = does not include Shanahan Conglomerate Member data, b = includes Shanahan Conglomerate Member data).

### 5.1.2. Lady Don Quartzite

Sample GSNSWKB001 was sampled from the Lady Don Quartzite in New South Wales. Based on its lithology and stratigraphic position, it is believed that this formation and the Christine Judith Conglomerate are equivalents to the basal Callanna Group. The maximum depositional age obtained for sample GSNSWKB001 is 1497 ± 52 Ma. There were a few zircons younger than this in the sample, with the youngest being 1302 ± 23 Ma. However, all younger zircons were slightly discordant (>2%, <10%). The sample's zircon age population is similar to that of the Paralana Quartzite (Figures 4 and 7) samples, with a primary population peak c. 1580 Ma, but includes an additional prominent population peak c. 1850 Ma. There were a few zircons with ages older than 2000 Ma, with one c. 3090 Ma, one c. 2670 Ma, and two c. 2450 Ma. The primary zircon population c. 1580 Ma was likely derived locally from the Ninnerie Supersuite and Radium Creek Group [79–82], lending support to stratigraphic correlation of the basal Adelaide Superbasin sequences (Figure 7). The additional population c. 1850 Ma was potentially derived from the underlying Willyama Supergroup [94,95], which has been suggested to ultimately be derived from the Arunta Province [96,97]. The few zircon grains older than 2000 Ma were also potentially derived from recycling of the underlying Willyama Supergroup. The rarity of these >2000 Ma zircons suggests that direct transport from the Gawler Craton where these ages were found, namely the Mulgathing Complex, Sleaford Complex, and Cooyerdoo Granite [83–85,98], is unlikely.

### 5.1.3. Cadlareena Volcanics

The small Cadlareena Volcanics sample, 3679330, only yielded 10 zircons that were all interpreted to be inherited/detrital, as there was significant spread with no apparent clustering in the individual ages (Figure 4), and most of the zircons were subhedral and fragmented. The sample's physical appearance suggests that the rock is a silicified, intermediate volcano-sedimentary rock. Therefore, this result is unsurprising. From this, we interpreted a maximum depositional age of 1189 ± 18 Ma. The ages of the zircon align with those found in the broader region, namely that of the Pitjantjatjara Supersuite of the Musgrave Province [87,99] and the Tunkillia Suite of the Gawler Craton [100–102].

### 5.1.4. Comparison to Basal Central Superbasin Sequences

The Centralian Superbasin developed as an intracontinental basin coeval with the Adelaide Superbasin [103,104], although the superbasins developed relatively independently from each other [25]. Geochronologic control, and thus correlation, of several stratigraphic units across the lower Adelaide Superbasin and Centralian Superbasin remain poor [10,105]. However, the lowermost units are commonly correlated based on stratigraphic similarity and position [24,41,103,105]. In the Centralian Superbasin, these formations are the Heavitree Formation, Dean Quartzite, Vaughn Springs Quartzite, Amesbury Quartzite, Munyu Sandstone, and Kulail Sandstone [105–107]. These are thought to be equivalents to the Adelaide Superbasin formations from which the samples analysed in this study were obtained. When the detrital zircon age populations were compared, two main groupings appeared, as the units of the Centralian Superbasin formed one group separate from those of the Adelaide Superbasin (Figure 7). This suggests that the two basins received detritus from differing sources. However, two exceptions occurred: the Heavitree Formation and the Shanahan Conglomerate Member. These two units both plotted (Figure 7) as an intermediary to the more obvious groupings of the Centralian Superbasin and Adelaide Superbasin sequences, suggesting a shared or similar primary detritus source. This is more easily explained for the Heavitree Formation, a relatively mature sandy unit, as the Arunta region, which has somewhat similar zircon age populations as the Gawler Craton, is inferred to be a major source of detritus for the Heavitree Formation [108,109]. This intermediary position in Figure 7 is much harder to reconcile for the Shanahan Conglomerate Member, as this unit is an immature breccia–conglomerate and is unlikely to have received detritus from distal sources. Moreover, as stated earlier, no local source of young zircon is known. This lends some support to the notion of a potential [27,91–93] Stenian–Tonian source to the east.

### *5.2. Zircon Trace Element Geochemistry*

Zircon trace element chemistry, particularly of the lanthanoids, uranium (U), thorium (Th), yttrium (Y), oxygen (O), and hafnium (Hf), can be useful in understanding their petrogenesis and provenance, and for crustal evolution [70,110–115]. Whereas lanthanoid geochemistry is not thought to be particularly useful in assisting with provenance determinations [116], it is useful at a broader scale for understanding the continental history of a region. Here, we make general observations about the trace element geochemistry of detrital zircon from the lowermost Adelaide Superbasin analysed in this study.

First, as a straightforward measure of continental or oceanic affinity for zircon generation, one can use U/Yb plotted against Y [112,113]. All zircons analysed in this study were inferred to have been generated in the continental crust, as shown by Figure 8. C1 chondrite-normalised [72] concentrations of lanthanoids are typical of zircon (Figure 5) with a positive pattern slope (decreasing λ1 values) from light to heavy lanthanoids, a positive cerium anomaly, and negative europium anomaly [116,117]. Nearly all zircons had a Th/U > 0.07 and were inferred to be originally generated as magmatic rather than metamorphic zircon [118,119]. There was no apparent trend in the lanthanoid pattern slope or curvature (Figure 9), denoted as λ1 (linear slope), λ2 (quadratic slope), and λ3 (cubic slope) [71], with time or sample. Both Eu and Ce anomalies (denoted by Eu* and Ce*) showed a significant spread through time. However, while statistical confidence is limited due to the low number of samples <1000 Ma, these samples generally had low Eu* and Ce* values ("low" is used as in [70], i.e., "strongly negative"). The positive correlation of low Eu* and Ce* values may suggest crystallisation in reduced conditions, thick crust, sediment incorporation, deep mantle plume, effects of fractional crystallisation, and/or competition with plagioclase and/or monazite [70]. The slight increase in Yb/U (Figure 9) in these younger zircons suggests the addition of MORB-like or juvenile mantle-derived magmatism, which is consistent with the type of magmatism accompanying Rodinia rifting.

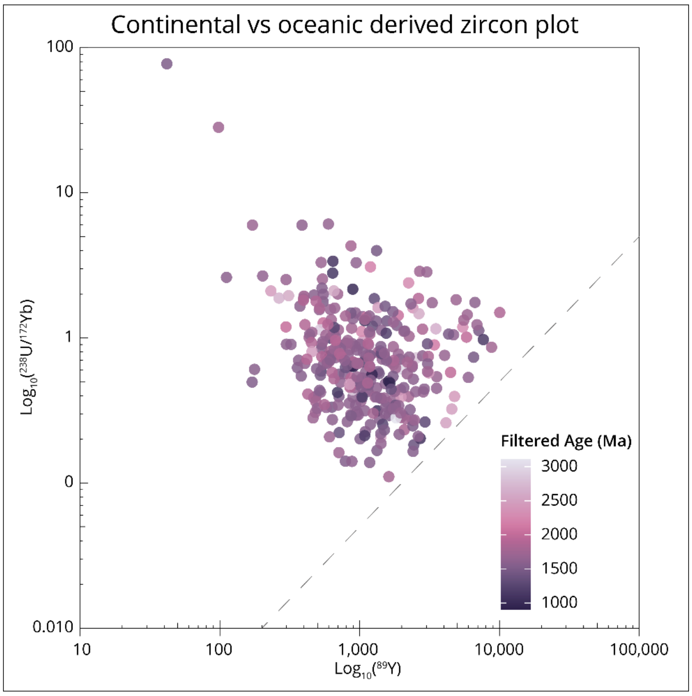

**Figure 8.** Plot based on [112] used as an indicator of zircon crustal origin. This plots Y against U/Yb, with the dashed reference line dividing the "oceanic" (below line) and "continental" (above line) fields. All data plotted above the reference line, suggesting zircon formation in the crust of continental affinity. Coloured by filtered age, where light is older and darker is younger.

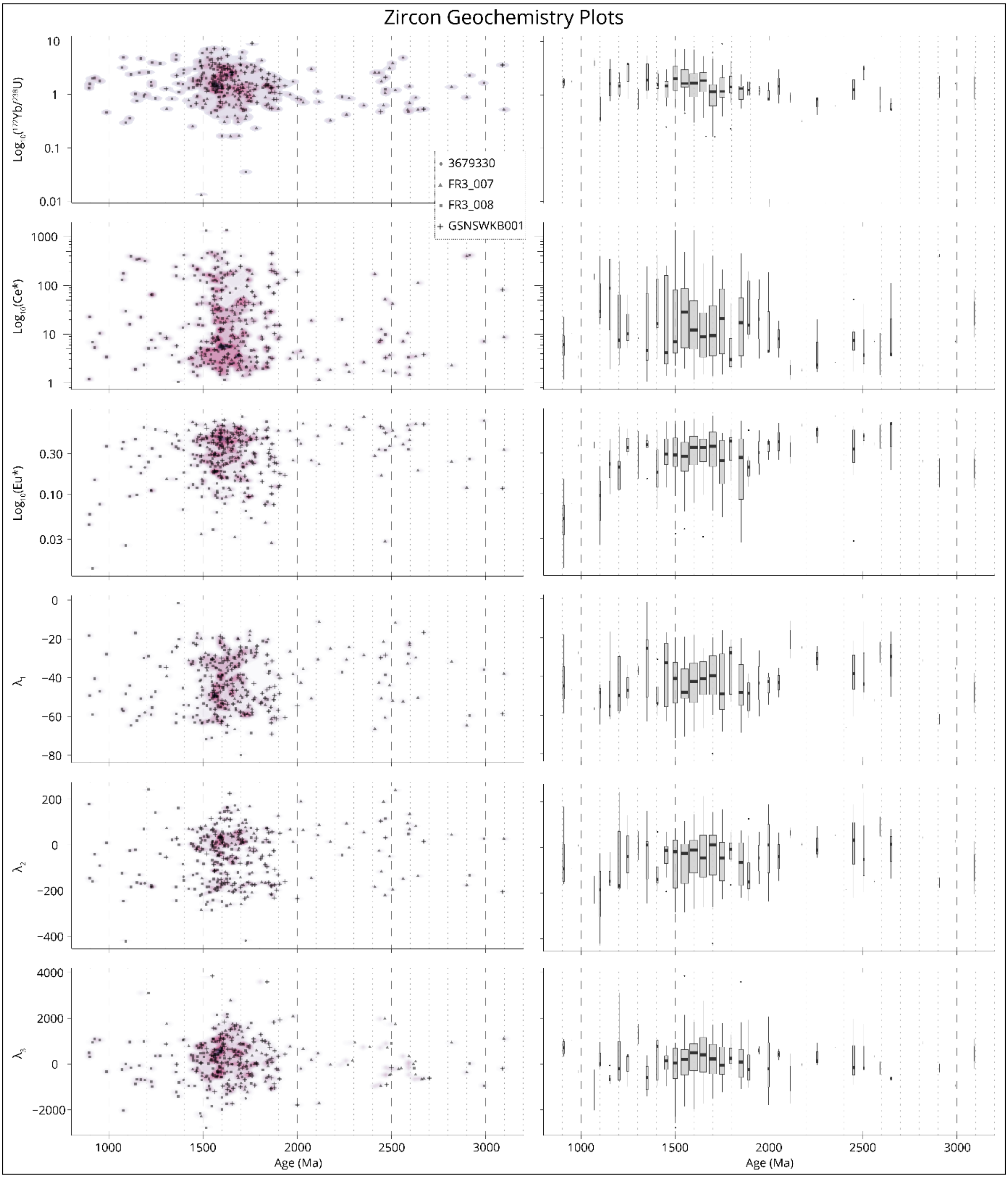

**Figure 9.** Key zircon geochemistry plots for zircon analysed in this study. Left: scatterplots underlain with 2D density estimation. Right: 50-million-year binned boxplots with width scaled by the count of values in the bin. Top to bottom: Yb/U, Ce*, Eu*, and λ1–3. λ1–3 are measures of lanthanoid pattern shapes, with λ1–3 representing the linear slope, quadratic slope, and cubic slope, respectively. Ce*, Eu*, and λ1–3 were calculated using BLambdaR [120].

### *5.3. Willouran Large Igneous Province and Palaeogeography*

Previous authors [20,27,48,121] have advocated for a spatial link of the Willouran Large Igneous Province (LIP) and the Guibei LIP primarily based on igneous geochemistry, palaeomagnetic poles, and geochronology. These authors have advocated for a link between southeast Proterozoic Australia and South China within Rodinia, known as the "missing link" model [20]. Wen and coauthors [21,22] developed an alternative missing link model placing Tarim between Australia and Laurentia instead of South China. However, an increasing number of studies examining detrital zircon, e.g., [122–125]; geodynamic and kinematic studies, e.g., [8,126,127]; and a recent comprehensive review and update to palaeomagnetic poles [128] have suggested that this position of South China (or Tarim) within the centre of Rodinia is unlikely. Further, this infers that the Willouran LIP and Guibei LIP are not spatially linked as previously suggested [20,27,48,51,121]. The new detrital zircon data in this study further support that the missing link model with Tarim or South China for Rodinia is unlikely. Our detrital zircon data (Figure 4) lack the prominent c. 800 Ma population that is present in samples from Tarim [122] and South China [124,129]. Our data also preserve prominent populations at c. 1580 Ma and c. 1840 Ma that are not prominent within samples from either Tarim or South China.

### *5.4. Early Evolution of the Adelaide Superbasin*

The majority of the Callanna Group has been either eroded, tectonically dismembered, or disrupted by diapirs, and geochronologic controls on deposition remain poor. There are also limited seismic surveys that cross the Adelaide Superbasin [130], and none cross key areas where good stratigraphic control of the Callanna Group is possible (e.g., Willouran Ranges). This makes reconstructing the earliest sequences of the Adelaide Superbasin and its evolution particularly difficult. Here, using existing research on the basin, drawing on literature concerning modern (e.g., East African Rift [131–137]) and ancient (e.g., Midcontinent Rift [138,139]) rift systems, and new detrital zircon data presented in this paper, we present an updated model for the early evolution of the Adelaide Superbasin.

Initiation of deposition within the Adelaide Superbasin (Figure 10) began between 893 ± 9 Ma and c. 830 Ma. The initial, thin, and geographically restricted, mostly brecciated/conglomeratic clastic sediments (e.g., Shanahan Conglomerate Member) were likely deposited in a series of small, somewhat asymmetric half-grabens with a local detrital source that contained enigmatic young (<1000 Ma) zircons. The half-grabens are thought to have developed by lithospheric thinning under an initial pulse of minor extension focused along pre-existing crustal weaknesses, e.g., Norwest Fault, Isan-Olarian orogen [27,95,140–145]. This initial extension was most probably a result of far-field forces [12], although a mantle plume may have played some role through thermal doming [146] or lithospheric weakening. Tectonic quiescence followed, with stable subsidence in the newly created rift, culminating with the deposition of alluvial to fluvial sands and shallow water, and sometimes stromatolitic carbonates (e.g., Paralana Quartzite, Wywyana Formation). This was initially reflected in the change in the zircon spectra of the Paralana Quartzite (Figure 4) to include a greater diversity of detrital sources before shallower water sediments were laid down. It is likely there was transtensional [28,147,148] movement along the Paralana Fault (and its splays) at this time, accounting for the significant thickness variation (~700 m) of the Paralana Quartzite across the fault plane in the Arkaroola area [24]. This interpretation differs from that of Preiss [25] but agrees with Mackay [27] and Job [28], in that we consider the Arkaroola Subgroup to be an early syn-rift, rather than pre-rift, deposition. However, it is worth noting that the amount of extension was minor. The Arkaroola Subgroup is here considered to reflect a sourceward-shifting facies tract (SFT) [53], which fines upward after the initial phase of rift basin development (Figures 3 and 10). Dyke emplacement (Gairdner Dolerite, Amata Dolerite) and extrusion of flood basalts (e.g., Wooltana Volcanics, Beda Basalt) occurs at the top of this first SFT and represents the first major phase of extension in the basin. The flood basalts were extruded in subaerial environments and may have originally formed a continuous sheet [24,25]. After extrusion of the Willouran LIP, rift development continued at an accelerated rate within well-developed grabens, with the deposition of cyclic clastic-carbonate-evaporative sequences of the Curdimurka Subgroup (Figures 3 and 11). This is consistent with detrital zircon and Nd provenance, suggesting a gradual transition from evolved to juvenile, and from broad to restricted detrital sources [10,149] over the long-term evolution of the basin. Evacuation of the magma chambers is thought to be partially responsible for the major graben subsidence [44]. The Curdimurka Subgroup is at least 8 km thick, much thicker than the Arkaroola Subgroup (Supplementary Figure S1), with significant variations across the basin (Figure 11). Magmatism is known to have continued during the deposition of the Curdimurka Subgroup, with bimodal volcanics known from the Willouran Ranges (Rook Tuff), a thin basalt flow in the Spalding Inlier, and xenoclasts of dolerite (thought to belong to the Curdimurka Subgroup) in diapirs/carbonate megabreccia zones [24]. Constraints on the end of Curdimurka Subgroup deposition, and thus the Callanna Group, remain poor. Whereas an exact stratigraphic position has not been determined due to a lack of intact contact relationships [58], the Oodla Wirra Volcanics provide the best determination of a maximum age for the final deposition of the Curdimurka Subgroup where two independent samples yielded ages of 798 ± 5 Ma and 799 ± 4 Ma [58]. This is within uncertainty of the 802 ± 10 Ma age of the Rook Tuff [150] of the lower to mid Curdimurka Subgroup. However, the age determination from the Rook Tuff needs revising as is not reproducible due to the unavailability of the isotopic data from the original analyses. In addition, increased precision and accuracy can be obtained on modern analytical equipment. The minimum age estimate for deposition of the Curdimurka Subgroup is constrained by the Boucaut Volcanics [151] and a porphyry in a basal member of the Skillogalee Dolomite [152] to c. 790 Ma. The exact stratigraphic position of the Boucaut Volcanics remains to be resolved [10]. However, the position of the Skillogalee Dolomite is well constrained. As such, the Callanna Group–Burra Group transition must have occurred between c. 800 Ma and c. 790 Ma and allowed for deposition of the upper Curdimurka Subgroup and entire Emeroo Subgroup. Deposition of the Emeroo Subgroup marks a southward propagation (Figure 12) of the Adelaide Rift Complex following upper Curdimurka Subgroup times. The most southerly deposition of the Curdimurka Subgroup occurred near Spalding [24,25], whereas deposition of the Burra Group occurred as far south as the Adelaide area (Figure 12). A renewed pulse of magmatism (e.g., Boucaut Volcanics, Jarrold Basalt Member, Kooringa Member) occurred at c. 790 Ma [151,152] in the southern and eastern areas of the basin, and likely marked a southern shift in tectonic activity and a period of tectonic quiescence of c. 70–80 million years in the northern Adelaide Superbasin.

In this model, the rift system did not develop as a classic triple junction system through apical extension as suggested by von der Borch [153] and Zhao et al. [154]. Instead, the northern and central areas of the Adelaide Rift Complex initiated as an intra-continental rift that formed along pre-existing crustal weakness and failed to progress to continental breakup, resulting in the present-day aulacogen (Figures 10–12). Later development of the Adelaide Rift Complex expanded the extent of the rift system to the south with wider deposition of the Burra Group. This southern region is suggested (Figure 12) to represent the successful rift axis of the Adelaide Superbasin where the proto-Pacific later formed, which is consistent with the kinematic constraints suggested by the authors of [8]. In this model, the triple junctions suggested by von der Borch [153] are a result of the intersection of propagating rifts to form a geometric triple junction.

This model is similar to recent ideas about the development of the Afar triple junction, where the Red Sea meets the Gulf of Aden and the East African Rift system. Traditionally, this area has been viewed as the classic triple junction rift-rift-rift system formed by apical extension away from the triple junction centre [155,156]. However, the geological evidence suggests that at least two of the three arms (Aden Rift, Ethiopian Rift) propagated inward toward the now-seen geometric triple junction, and the chronology of the rift systems does not fit with plume driven apical extension from a central point, e.g., [132,135,136,157]. It appears that the modern Afar triple junction is a geometric place where three rifts, with their predetermined geometries, happened to cross rather than being the point of initiation, e.g., [132,135,136,157], similar to our model for the Adelaide Rift Complex.

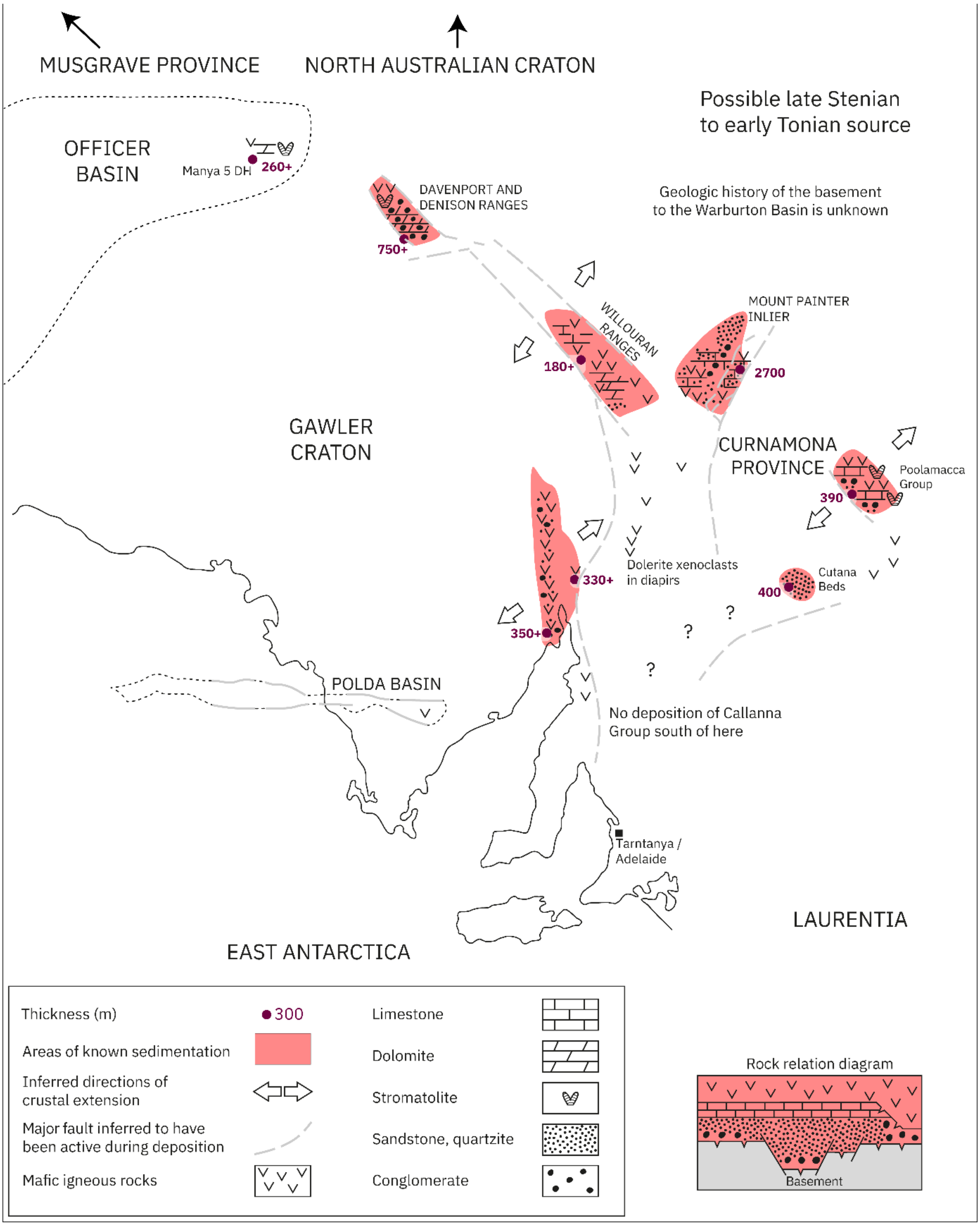

**Figure 10.** Paleogeographic map showing the known distribution of the Arkaroola Subgroup (c. 890–830 Ma) sedimentary deposition. Relative positions of relevant continental blocks in Rodinia are also indicated. Dolerite xenoclasts in diapiric breccia are likely related to the Gairdner Dyke Swarm of the Willouran LIP (see Figure 3). Deposition of Arkaroola Subgroup rocks may have occurred in regions between the indicated areas, However, this is not confirmed. Geography of the Adelaide Superbasin is shown in its modern-day configuration, with the modern coastline shown for reference. Adapted from Preiss [41].

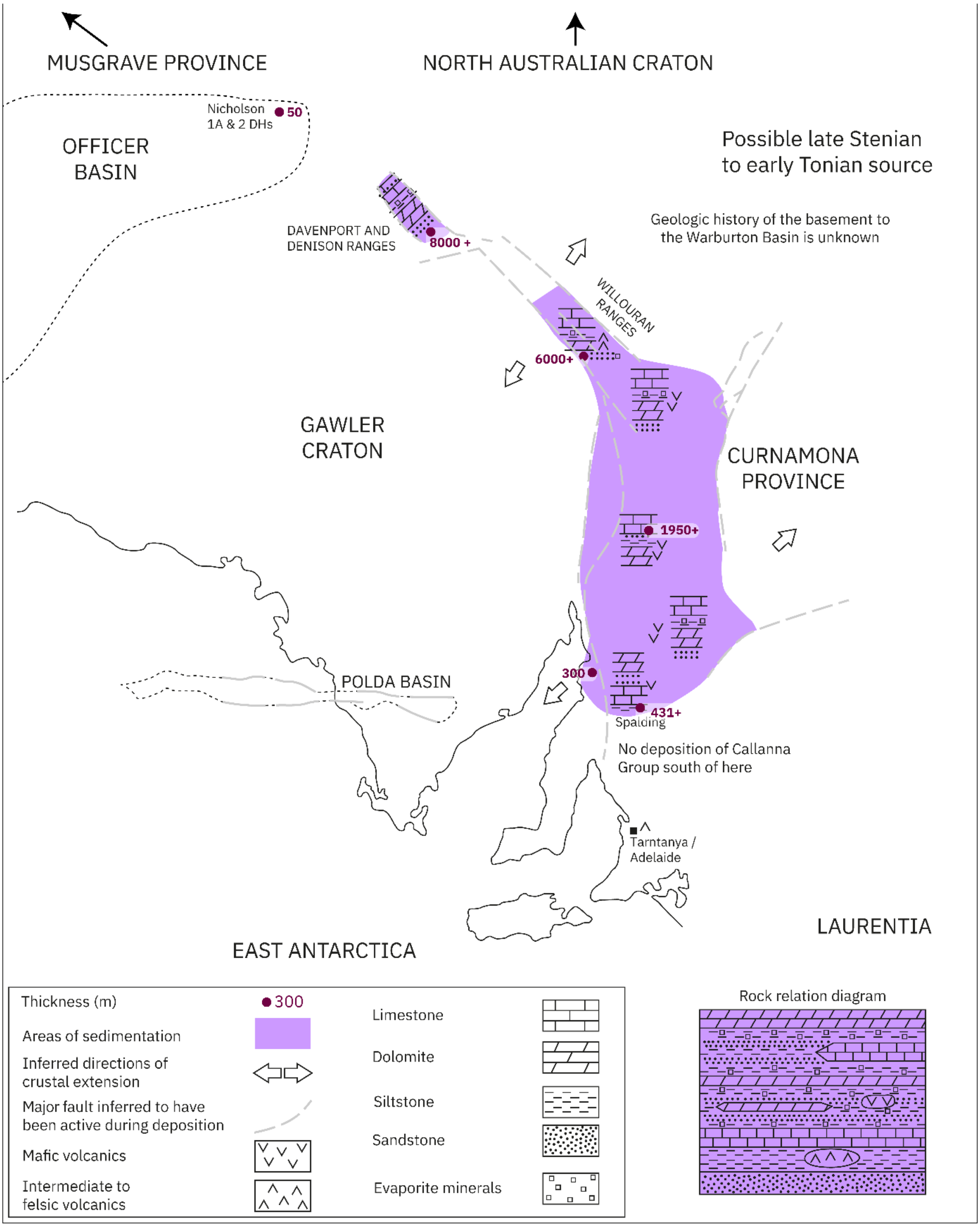

**Figure 11.** Paleogeographic map showing the known distribution of the Curdimurka Subgroup (c. 830–800 Ma) sedimentary deposition. Relative positions of relevant continental blocks in Rodinia are also indicated. Geography of the Adelaide Superbasin is shown in its modern-day configuration, with the modern coastline shown for reference. Adapted from Preiss [41].

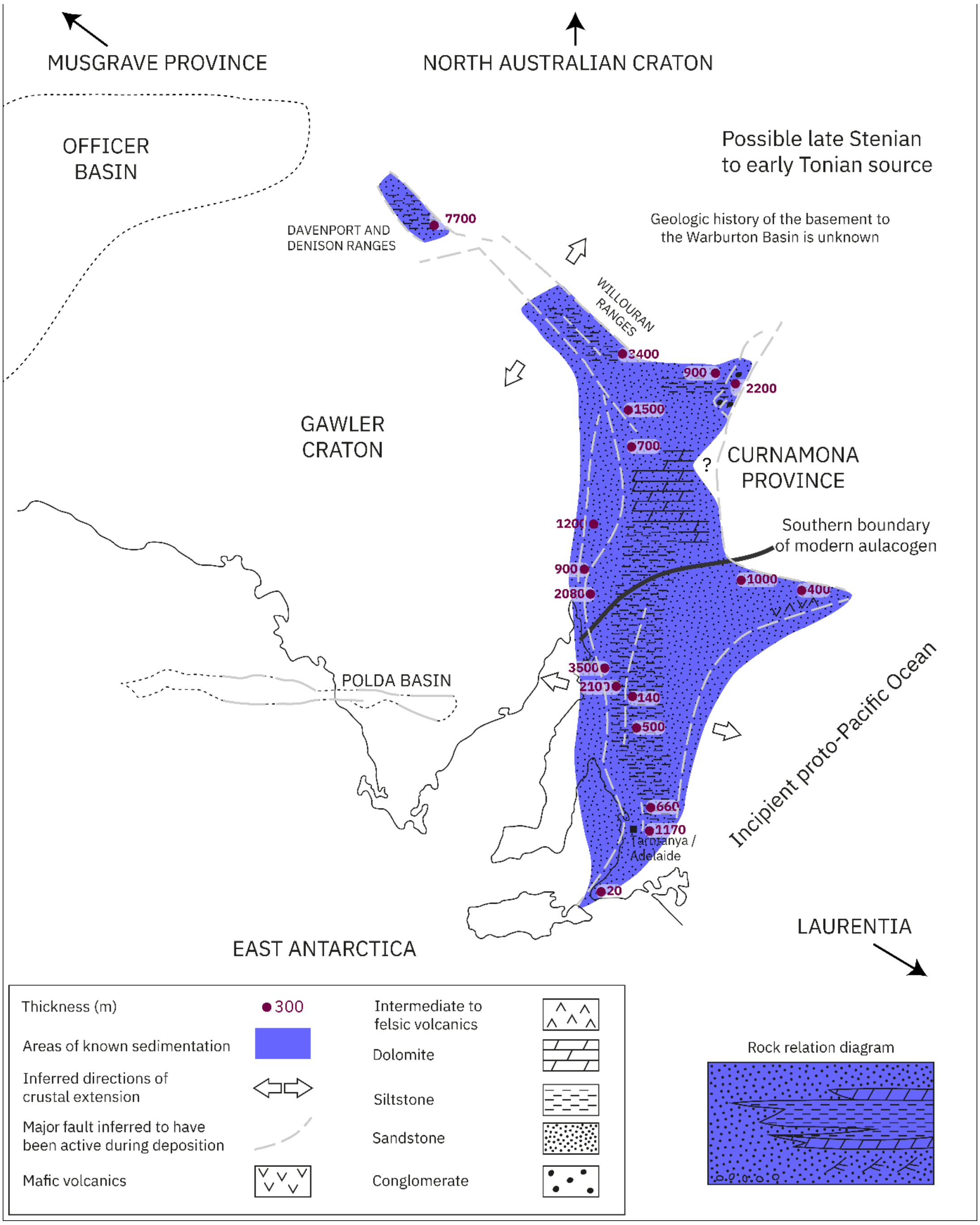

**Figure 12.** Paleogeographic map showing the known distribution of the Emeroo Subgroup (c. 800–790 Ma) sedimentary deposition, highlighting the southward progression of deposition (and the rift system) in the Adelaide Superbasin. Relative positions of relevant continental blocks in Rodinia are also indicated. Geography of the Adelaide Superbasin is shown in its modern-day configuration, with the modern coastline shown for reference. Adapted from Preiss [41].

## 6. Conclusions

The development of the Adelaide Superbasin initiated between c. 890–830 Ma with the deposition of the Arkaroola Subgroup in a series of structurally controlled half-grabens in what now constitutes the Adelaide Rift Complex. These structures are likely a manifestation of northeast-southwest (present day)-orientated extensional strain from far-field forces, and potentially also stress from a mantle plume. This phase of extension was limited, and tectonic quiescence followed until extrusion of the Willouran Large Igneous Province (LIP).

The Willouran LIP may have been the result of a mantle plume, and its emplacement led to extensive rifting and the subsequent deposition of the Curdimurka Subgroup.

The key findings of this research are:

- Revised constraints on the timing of initial deposition within the Adelaide Superbasin, between ≥893 ± 9 Ma and c. 830 Ma.
- The identification of an enigmatic source of young (<1000 Ma) zircon in the basal stratigraphic unit.
- The Arkaroola Subgroup represents early, syn-rift deposition within half-grabens, developed in an initial pulse of extension that likely exploited pre-existing crustal weakness.
- The central and northern Flinders Ranges formed the initial arm of the rift system but failed to progress to continental breakup.
- Basal Centralian Superbasin and Adelaide Superbasin stratigraphic units had different primary detrital sources.
- Support for a potential late Mesoproterozoic source region to the east of the basin.

**Supplementary Materials:** Supplementary Figure S1 is available as both an EPS file and a PNG file hosted on Figshare: https://doi.org/10.6084/m9.figshare.19153274.

**Author Contributions:** J.C.L.: Conceptualisation, investigation, writing—original draft, writing—review & editing, methodology, formal analysis, data curation, visualisation. M.L.B.: Investigation, writing—review & editing. A.S.C.: Conceptualisation, funding acquisition, supervision, investigation, writing—review & editing. S.E.G.: Formal analysis, methodology, investigation, writing—review & editing. K.J.A.: Conceptualisation, funding acquisition, supervision, writing—review & editing. All authors have read and agreed to the published version of the manuscript.

**Funding:** The Geological Survey of South Australia and the MinEx CRC funded this research. This research was supported by an Australian Government Research Training Program (RTP) Scholarship awarded to JCL.

**Data Availability Statement:** Complete data for this publication are freely available for download from Figshare at the following links. These datasets contain all the U–Pb geochronology data, trace element data, and basic sample metadata. Zircon and NIST standards data for all analytical sessions: https://doi.org/10.6084/m9.figshare.18131432 [158]. Callanna Group (this study only) detrital zircon data: https://doi.org/10.6084/m9.figshare.18131420 [159]. The R code used to generate the zircon geochemistry plots is available on GitHub at https://github.com/jarredclloyd/zircon-trace-element-plots (accessed on 10 February 2022).

**Acknowledgments:** We acknowledge the Adnyamathanha, Arabana, Banggarla, Kaurna, Kokatha, Kuyani, Ngadjuri, and Nukunu Peoples as the Traditional Owners and Custodians of the land on which this research was conducted. We acknowledge and respect their deep feelings of attachment and spiritual relationship to the Country, and that their cultural and heritage beliefs are still as important to the living people today. The authors acknowledge the instruments and scientific and technical assistance of Microscopy Australia at Adelaide Microscopy, the University of Adelaide, a facility that is funded by the University, and state and federal governments. We give particular thanks to Aoife McFadden for their assistance with CL imaging. We also thank Wolfgang Preiss (Geological Survey of South Australia; University of Adelaide) for his expertise on the Adelaide Superbasin, James Nankivell, and Georgina Virgo (University of Adelaide) for their assistance with fieldwork. Chris Folkes (Geological Survey of New South Wales) and John Greenfield (formerly GSNSW) are thanked for sharing expertise of the New South Wales sequences. The authors thank all reviewers for their comments that strengthen this manuscript.

**Conflicts of Interest:** The authors declare no conflict of interest. This work is conducted with the appropriate permissions and scientific permits from the relevant stakeholders.

## Appendix A. Use of NIST610 as Primary $^{207}$Pb/$^{206}$Pb Standard

Matrix matched reference materials are essential for the accurate determination of U/Pb ratios, and thus calculated ages, of accessory minerals such as zircon via laser ablation mass spectrometry [160–163]. This is due to the offset in ratio and subsequently age determinations caused by “matrix effects” [164–166]. Primarily, this is a result of down-hole fractionation [167,168] with one of the major causes being laser induced elemental fractionation (LIEF) of U from Pb in the crystal lattice [164,165]. However, it has been determined that there is negligible to no fractionation of Pb isotopes during laser ablation of various accessory minerals and silicate glasses [162,163,169,170], thus allowing the use of non-matrix matched silicate glasses (e.g., NIST610) as external reference materials for the determination of accurate Pb isotope ratios. Methodology using NIST610, or other silicate glasses, as the $^{207}$Pb/$^{206}$Pb primary reference material has been successfully used in past [170–173]. We further validate this as the NIST610 corrected $^{207}$Pb/$^{206}$Pb ratio and calculated age for every natural zircon reference material analysed is within uncertainty at high accuracy [Figure A1] of their CA-ID-TIMS determined values [63]. The use of NIST610 allows for more precise determination of Pb isotope ratios due to the better homogeneity and characterisation of the reference material [67] while retaining accuracy. This is useful in overcoming the higher degrees of uncertainty associated with natural reference materials that are measurably heterogenous [63,174], which is likely the result of radiation damage induced lead loss, zonation in zircon crystallinity, or protracted growth.

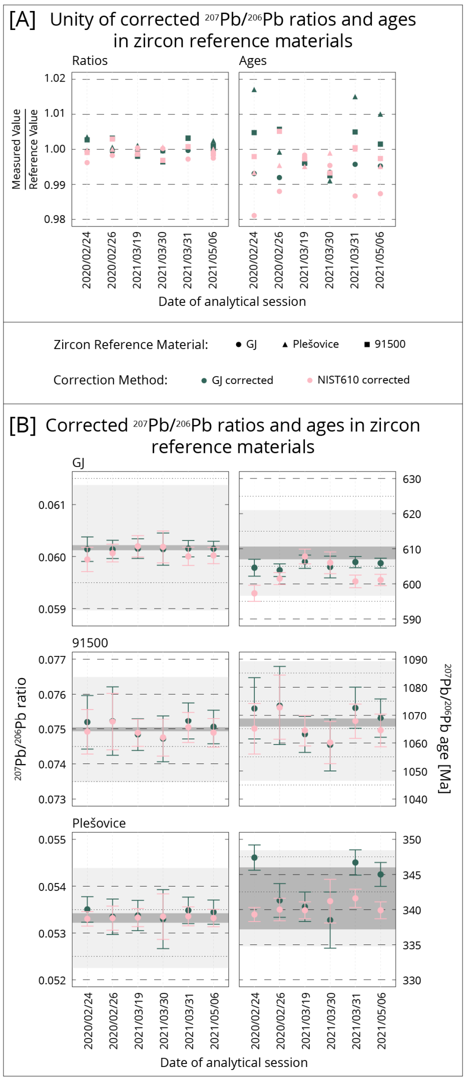

**Figure A1.** (**A**) Unity measure (observed/reference value) of corrected Pb isotope ratios and ages. (**B**) individual observed corrected ratios and ages for each natural zircon reference material used. Dark grey shading is the reference value range (2× standard error), light grey shading is the 2% unity range (reference value ± 2%). Uncertainties on observations are 2 standard error. Refence values are from [63].

## References

1. Halverson, G.P.; Hurtgen, M.T.; Porter, S.M.; Collins, A.S. Neoproterozoic-Cambrian Biogeochemical Evolution. In *Developments in Precambrian Geology*; Gaucher, C., Sial, A.N., Frimmel, H.E., Halverson, G.P., Eds.; Elsevier: Amsterdam, The Netherlands, 2009; Volume 16, pp. 351–365.
2. Shields, G.A.; Strachan, R.A.; Porter, S.M.; Halverson, G.P.; Macdonald, F.A.; Plumb, K.A.; de Alvarenga, C.J.; Banerjee, D.M.; Bekker, A.; Bleeker, W.; et al. A template for an improved rock-based subdivision of the pre-Cryogenian timescale. *J. Geol. Soc.* **2021**, 179. [CrossRef]
3. Tostevin, R.; Mills, B.J.W. Reconciling proxy records and models of Earth's oxygenation during the Neoproterozoic and Palaeozoic. *Interface Focus* **2020**, *10*, 20190137. [CrossRef] [PubMed]
4. Alcott, L.J.; Krause, A.J.; Hammarlund, E.U.; Bjerrum, C.J.; Scholz, F.; Xiong, Y.; Hobson, A.J.; Neve, L.; Mills, B.J.W.; März, C.; et al. Development of Iron Speciation Reference Materials for Palaeoredox Analysis. *Geostand. Geoanal. Res.* **2020**, *44*, 581–591. [CrossRef]
5. Gernon, T.M.; Hincks, T.K.; Tyrrell, T.; Rohling, E.J.; Palmer, M.R. Snowball Earth ocean chemistry driven by extensive ridge volcanism during Rodinia breakup. *Nat. Geosci.* **2016**, *9*, 242–248. [CrossRef]
6. Mills, B.J.W.; Krause, A.J.; Scotese, C.R.; Hill, D.J.; Shields, G.A.; Lenton, T.M. Modelling the long-term carbon cycle, atmospheric CO2, and Earth surface temperature from late Neoproterozoic to present day. *Gondwana Res.* **2019**, *67*, 172–186. [CrossRef]
7. Merdith, A.S.; Williams, S.E.; Collins, A.S.; Tetley, M.G.; Mulder, J.A.; Blades, M.L.; Young, A.; Armistead, S.E.; Cannon, J.; Zahirovic, S.; et al. Extending full-plate tectonic models into deep time: Linking the Neoproterozoic and the Phanerozoic. *Earth-Sci. Rev.* **2021**, *214*, 103477. [CrossRef]
8. Merdith, A.S.; Williams, S.E.; Müller, R.D.; Collins, A.S. Kinematic constraints on the Rodinia to Gondwana transition. *Precambrian Res.* **2017**, *299*, 132–150. [CrossRef]
9. Collins, A.S.; Blades, M.L.; Merdith, A.S.; Foden, J.D. Closure of the Proterozoic Mozambique Ocean was instigated by a late Tonian plate reorganization event. *Commun. Earth Environ.* **2021**, *2*, 75. [CrossRef]
10. Lloyd, J.C.; Blades, M.L.; Counts, J.W.; Collins, A.S.; Amos, K.J.; Wade, B.P.; Hall, J.W.; Hore, S.; Ball, A.L.; Shahin, S.; et al. Neoproterozoic geochronology and provenance of the Adelaide Superbasin. *Precambrian Res.* **2020**, *350*, 105849. [CrossRef]
11. Bogdanova, S.V.; Pisarevsky, S.A.; Li, Z.-X. Assembly and Breakup of Rodinia (Some results of IGCP project 440). *Stratigr. Geol. Correl.* **2009**, *17*, 259–274. [CrossRef]
12. Cawood, P.A.; Strachan, R.A.; Pisarevsky, S.A.; Gladkochub, D.P.; Murphy, J.B. Linking collisional and accretionary orogens during Rodinia assembly and breakup: Implications for models of supercontinent cycles. *Earth Planet. Sci. Lett.* **2016**, *449*, 118–126. [CrossRef]
13. Li, Z.-X.; Bogdanova, S.V.; Collins, A.S.; Davidson, A.; De Waele, B.; Ernst, R.E.; Fitzsimons, I.C.W.; Fuck, R.A.; Gladkochub, D.P.; Jacobs, J.; et al. Assembly, configuration, and break-up history of Rodinia: A synthesis. *Precambrian Res.* **2008**, *160*, 179–210. [CrossRef]
14. Brookfield, M.E. Neoproterozoic Laurentia-Australia fit. *Geology* **1993**, *21*, 683–686. [CrossRef]
15. Dalziel, I.W.D. OVERVIEW: Neoproterozoic-Paleozoic geography and tectonics: Review, hypothesis, environmental speculation. *GSA Bull.* **1997**, *109*, 16–42. [CrossRef]
16. Hoffman, P.F. Did the Breakout of Laurentia Turn Gondwanaland Inside-Out? *Science* **1991**, *252*, 1409–1412. [CrossRef] [PubMed]
17. Karlstrom, K.E.; Harlan, S.S.; Williams, M.L.; McLelland, J.; Geissman, J.W.; Ahäll, K.-I. Refining Rodinia: Geologic evidence for the Australia-western US connection in the Proterozoic. *GSA Today* **1999**, *9*, 1–7. [CrossRef]
18. Moores, E.M. Southwest U.S.-East Antarctic (SWEAT) connection: A hypothesis. *Geology* **1991**, *19*, 425–428. [CrossRef]
19. Wingate, M.T.D.; Pisarevsky, S.A.; Evans, D.A.D. Rodinia connections between Australia and Laurentia: No SWEAT, no AUSWUS? *Terra Nova* **2002**, *14*, 121–128. [CrossRef]
20. Li, Z.-X.; Zhang, L.; Powell, C.M. South China in Rodinia: Part of the missing link between Australia–East Antarctica and Laurentia? *Geology* **1995**, *23*, 407–410. [CrossRef]
21. Wen, B.; Evans, D.A.D.; Li, Y.-X. Neoproterozoic paleogeography of the Tarim Block: An extended or alternative "missing-link" model for Rodinia? *Earth Planet. Sci. Lett.* **2017**, *458*, 92–106. [CrossRef]
22. Wen, B.; Evans, D.A.D.; Wang, C.; Li, Y.-X.; Jing, X. A positive test for the Greater Tarim Block at the heart of Rodinia: Mega-dextral suturing of supercontinent assembly. *Geology* **2018**, *46*, 687–690. [CrossRef]
23. Sprigg, R.C. Sedimentation in the Adelaide Geosyncline and the formation of the continental terrace. In *Sir Douglas Mawson Anniversary Volume*; Glaessner, M.F., Sprigg, R.C., Eds.; The University of Adelaide: Adelaide, Australia, 1952; pp. 153–159.
24. Preiss, W.V. *Adelaide Geosyncline—Late Proterozoic Stratigraphy, Sedimentation, Palaeontology and Tectonics*; Drexel, J.F., Ed.; Geological Survey of South Australia: Adelaide, Australia, 1987; p. 428.
25. Preiss, W.V. The Adelaide Geosyncline of South Australia and its significance in Neoproterozoic continental reconstruction. *Precambrian Res.* **2000**, *100*, 21–63. [CrossRef]
26. Counts, J.W. Sedimentology, Provenance, and Salt-Sediment Interaction in the Ediacaran Pound Subgroup, Flinders Ranges, South Australia. Ph.D. Thesis, University of Adelaide, Adelaide, South Australia, 2016.
27. Mackay, W.G. Structure and Sedimentology of the Curdimurka Subgroup, Northern Adelaide Fold Belt, South Australia. Ph.D. Thesis, University of Tasmania, Hobart, Tasmania, 2011.

28. Job, A.L. Evolution of the Basal Adelaidean in the Northern Flinders Ranges: Deposition, Provenance and Deformation of the Callanna and Lower Burra Groups. Ph.D. Thesis, University of Adelaide, Adelaide, South Australia, 2011.
29. Keeman, J.; Turner, S.; Haines, P.W.; Belousova, E.; Ireland, T.; Brouwer, P.; Foden, J.; Wörner, G. New UPb, Hf and O isotope constraints on the provenance of sediments from the Adelaide Rift Complex—Documenting the key Neoproterozoic to early Cambrian succession. *Gondwana Res.* **2020**, *83*, 248–278. [CrossRef]
30. Callen, R.A. *Curnamona*; Department of Mines and Energy: Adelaide, Australia, 1990; p. 56.
31. Preiss, W.V.; Alexander, E.M.; Cowley, W.M.; Schwarz, M.P. Towards defining South Australia's geological provinces and sedimentary basins. *MESA J.* **2002**, *27*, 39–52.
32. Mulder, J.A.; Berry, R.F.; Halpin, J.A.; Meffre, S.; Everard, J.L. Depositional age and correlation of the Oonah Formation: Refining the timing of Neoproterozoic basin formation in Tasmania. *Aust. J. Earth Sci.* **2018**, *65*, 391–407. [CrossRef]
33. Drexel, J.F.; Preiss, W.V. (Eds.) *The Geology of South Australia*; Geological Survey of South Australia: Adelaide, Australia, 1995; Volume 2.
34. Foden, J.D.; Elburg, M.A.; Dougherty-Page, J.; Burtt, A. The timing and duration of the Delamerian orogeny: Correlation with the Ross Orogen and implications for Gondwana assembly. *J. Geol.* **2006**, *114*, 189–210. [CrossRef]
35. Foden, J.D.; Elburg, M.A.; Turner, S.; Clark, C.; Blades, M.L.; Cox, G.; Collins, A.S.; Wolff, K.; George, C. Cambro-Ordovician magmatism in the Delamerian orogeny: Implications for tectonic development of the southern Gondwanan margin. *Gondwana Res.* **2020**, *81*, 490–521. [CrossRef]
36. Counts, J.W. *The Adelaide Rift Complex in the Flinders Ranges: Geologic history, Past Investigations and Relevant Analogues*; Report Book 2017/00016; Geological Survey of South Australia: Adelaide, Australia, 2017; p. 47.
37. Cowley, W.M. Geological setting of exceptional geological features of the Flinders Ranges. *Aust. J. Earth Sci.* **2020**, *67*, 763–785. [CrossRef]
38. Forbes, B.G.; Murrell, B.; Preiss, W.V. Subdivision of lower Adelaidean, Willouran Ranges. *Q. Geol. Notes* **1981**, *79*, 7–16.
39. Thomson, B.P. The lower boundary of the Adelaide system and older basement relationships in south Australia. *J. Geol. Soc. Aust.* **1966**, *13*, 203–228. [CrossRef]
40. Mawson, D. Sturtian tillite of Mount Jacob and Mount Warren Hastings, north Flinders Ranges. *Trans. Roy. Soc. S. Aust.* **1949**, *72*, 244–251.
41. Preiss, W.V. Neoproterozoic. In *The Geology of South Australia*; Drexel, J.F., Preiss, W.V., Parker, A.J., Eds.; Bulletin; Geological Survey of South Australia: Adelaide, Australia, 1993; Volume 1, pp. 171–204.
42. Cooper, P.F.; Tuckwell, K.D. The upper Precambrian Adelaidean of the Broken Hill area—A new subdivision. *Q. Notes-Geol. Surv. N. S. W.* **1971**, *3*, 8–16.
43. Coats, R.P.; Blissett, A.H. *Regional and Economic Geology of the Mount Painter Province*; Geological Survey of South Australia: Adelaide, Australia, 1971.
44. Hillyard, D. Willouran Basic Province: Stratigraphy of Late Proterozoic flood basalts, Adelaide Geosyncline, South Australia. In *The Evolution of a Late Precambrian Early Palaeozoic Rift Complex: The Adelaide Geosyncline*; Special Publication (No. 16); Jago, J.B., Moore, P.S., Eds.; Geological Society of Australia Inc.: Sydney, Australia, 1990; pp. 34–48.
45. Crawford, A.J.; Hillyard, D. Geochemistry of Late Proterozoic tholeiitic flood basalts, Adelaide Geosyncline, South Australia. In *The Evolution of a Late Precambrian Early Palaeozoic Rift Complex: The Adelaide Geosyncline*; Special Publication (No. 16); Jago, J.B., Moore, P.S., Eds.; Geological Society of Australia Inc.: Sydney, Australia, 1990; pp. 49–67.
46. Powell, C.M. Assembly and Break-up of Rodinia Leading to Formation of Gondwana Land. In *The Assembly and Breakup of Rodinia*; Bird, R.T., Ed.; Geological Society of Australia Abstracts; Geological Society of Australia: Sydney, Australia, 1998; pp. 49–53.
47. Wade, C.E.; McAvaney, S.O.; Gordan, G.A. The Beda Basalt: New geochemistry, isotopic data and its definition. *MESA J.* **2014**, *73*, 24–39.
48. Wang, X.-C.; Li, X.-H.; Li, Z.-X.; Liu, Y.; Yang, Y.-H. The Willouran basic province of South Australia: Its relation to the Guibei large igneous province in South China and the breakup of Rodinia. *Lithos* **2010**, *119*, 569–584. [CrossRef]
49. Wingate, M.T.D.; Campbell, I.H.; Compston, W.; Gibson, G.M. Ion microprobe U–Pb ages for Neoproterozoic basaltic magmatism in south-central Australia and implications for the breakup of Rodinia. *Precambrian Res.* **1998**, *87*, 135–159. [CrossRef]
50. Huang, Q.; Kamenetsky, V.S.; McPhie, J.; Ehrig, K.; Meffre, S.; Maas, R.; Thompson, J.; Kamenetsky, M.; Chambefort, I.; Apukhtina, O.; et al. Neoproterozoic (ca. 820–830Ma) mafic dykes at Olympic Dam, South Australia: Links with the Gairdner Large Igneous Province. *Precambrian Res.* **2015**, *271*, 160–172. [CrossRef]
51. Werner, M.; Dutch, R.A.; Pawley, M.J.; Krapf, C.B.E. Amata Dolerite, Musgrave Province: Connections to Neoproterozoic mantle plume magmatism within Rodinia. *MESA J.* **2018**, *87*, 34–45.
52. Travers, D.C. Geochronology, Geochemistry and Petrogenesis of Mafic Magmatism in the Coompana Province. Ph.D. Thesis, University of Adelaide, Adelaide, Australia, 2015.
53. Matenco, L.C.; Haq, B.U. Multi-scale depositional successions in tectonic settings. *Earth-Sci. Rev.* **2020**, *200*, 102991. [CrossRef]
54. Ambrose, G.J.; Flint, R.B.; Webb, A.W. *Precambrian and Palaeozoic Geology of the Peake and Denison Ranges*; Geological Survey of South Australia: Adelaide, Australia, 1981; p. 73.
55. Hearon IV, T.E.; Rowan, M.G.; Lawton, T.F.; Hannah, P.T.; Giles, K.A. Geology and tectonics of Neoproterozoic salt diapirs and salt sheets in the eastern Willouran Ranges, South Australia. *Basin Res.* **2015**, *27*, 183–207. [CrossRef]

56. Preiss, W.V. *Stratigraphy and Tectonics of the Worumba Anticline and Associated Intrusive Breccias*; Geological Survey of South Australia: Adelaide, Australia, 1985.
57. Preiss, W.V. The River Broughton Beds-a Willouran sequence in the Spalding inlier. *Q. Geol. Notes* **1974**, *49*, 2–8.
58. Fabris, A.J.; Constable, S.A.; Conor, C.H.H.; Woodhouse, A.; Hore, S.B.; Fanning, M. Age, origin, emplacement and mineral potential of the Oodla Wirra Volcanics, Nackara Arc, central Flinders Ranges. *MESA J.* **2005**, *37*, 44–52.
59. Stüeken, E.E.; Buick, R.; Lyons, T.W. Revisiting the depositional environment of the Neoproterozoic Callanna Group, South Australia. *Precambrian Res.* **2019**, *334*, 105474. [CrossRef]
60. Sláma, J.; Košler, J. Effects of sampling and mineral separation on accuracy of detrital zircon studies. *Geochem. Geophys. Geosystems* **2012**, *13*, Q05007. [CrossRef]
61. Dröllner, M.; Barham, M.; Kirkland, C.L.; Ware, B. Every zircon deserves a date: Selection bias in detrital geochronology. *Geol. Mag.* **2021**, *158*, 1135–1142. [CrossRef]
62. Jackson, S.E.; Pearson, N.J.; Griffin, W.L.; Belousova, E.A. The application of laser ablation-inductively coupled plasma-mass spectrometry to in situ U–Pb zircon geochronology. *Chem. Geol.* **2004**, *211*, 47–69. [CrossRef]
63. Horstwood, M.S.A.; Košler, J.; Gehrels, G.E.; Jackson, S.E.; McLean, N.M.; Paton, C.; Pearson, N.J.; Sircombe, K.N.; Sylvester, P.; Vermeesch, P.; et al. Community-Derived Standards for LA-ICP-MS U-(Th-)Pb Geochronology-Uncertainty Propagation, Age Interpretation and Data Reporting. *Geostand. Geoanal. Res.* **2016**, *40*, 311–332. [CrossRef]
64. Sláma, J.; Košler, J.; Condon, D.J.; Crowley, J.L.; Gerdes, A.; Hanchar, J.M.; Horstwood, M.S.A.; Morris, G.A.; Nasdala, L.; Norberg, N.; et al. Plešovice zircon—A new natural reference material for U–Pb and Hf isotopic microanalysis. *Chem. Geol.* **2008**, *249*, 1–35. [CrossRef]
65. Wiedenbeck, M.; Allé, P.; Corfu, F.; Griffin, W.L.; Meier, M.; Oberli, F.; Quadt, A.V.; Roddick, J.C.; Spiegel, W. Three Natural Zircon Standards for U-Th-Pb, Lu-Hf, Trace Element and REE Analyses. *Geostand. Newslett.* **1995**, *19*, 1–23. [CrossRef]
66. Wiedenbeck, M.; Hanchar, J.M.; Peck, W.H.; Sylvester, P.; Valley, J.; Whitehouse, M.; Kronz, A.; Morishita, Y.; Nasdala, L.; Fiebig, J.; et al. Further Characterisation of the 91500 Zircon Crystal. *Geostand. Geoanal. Res.* **2004**, *28*, 9–39. [CrossRef]
67. Jochum, K.P.; Weis, U.; Stoll, B.; Kuzmin, D.; Yang, Q.; Raczek, I.; Jacob, D.E.; Stracke, A.; Birbaum, K.; Frick, D.A.; et al. Determination of Reference Values for NIST SRM 610–617 Glasses Following ISO Guidelines. *Geostand. Geoanal. Res.* **2011**, *35*, 397–429. [CrossRef]
68. Norris, A.; Danyushevsky, L. Towards Estimating the Complete Uncertainty Budget of Quantified Results Measured by LA-ICP-MS. In Proceedings of the Goldschmidt, Boston, MA, USA, 12–17 August 2018.
69. Vermeesch, P. IsoplotR: A free and open toolbox for geochronology. *Geosci. Front.* **2018**, *9*, 1479–1493. [CrossRef]
70. Verdel, C.; Campbell, M.J.; Allen, C.M. Detrital zircon petrochronology of central Australia, and implications for the secular record of zircon trace element composition. *Geosphere* **2021**, *17*, 538–560. [CrossRef]
71. Anenburg, M. Rare earth mineral diversity controlled by REE pattern shapes. *Mineral. Mag.* **2020**, *84*, 629–639. [CrossRef]
72. O'Neill, H.S.C. The Smoothness and Shapes of Chondrite-normalized Rare Earth Element Patterns in Basalts. *J. Petrol.* **2016**, *57*, 1463–1508. [CrossRef]
73. Shannon, R.D. Revised effective ionic radii and systematic studies of interatomic distances in halides and chalcogenides. *Acta Crystallogr. Sect. A* **1976**, *32*, 751–767. [CrossRef]
74. Vermeesch, P.; Resentini, A.; Garzanti, E. An R package for statistical provenance analysis. *Sediment. Geol.* **2016**, *336*, 14–25. [CrossRef]
75. Corfu, F.; Hanchar, J.M.; Hoskin, P.W.O.; Kinny, P. Atlas of zircon textures. *Rev. Mineral. Geochem.* **2003**, *53*, 469–500. [CrossRef]
76. Pupin, J.P. Zircon and granite petrology. *Contrib. Mineral. Petrol.* **1980**, *73*, 207–220. [CrossRef]
77. Ludwig, K.R. On the Treatment of Concordant Uranium-Lead Ages. *Geochim. Cosmochim. Acta* **1998**, *62*, 665–676. [CrossRef]
78. Vermeesch, P. On the treatment of discordant detrital zircon U–Pb data. *Geochronology* **2021**, *3*, 247–257. [CrossRef]
79. Armit, R.J.; Betts, P.G.; Schaefer, B.F.; Pankhurst, M.J.; Giles, D. Provenance of the Early Mesoproterozoic Radium Creek Group in the northern Mount Painter Inlier: Correlating isotopic signatures to inform tectonic reconstructions. *Precambrian Res.* **2014**, *243*, 63–87. [CrossRef]
80. Wade, C.E. Definition of the Mesoproterozoic Ninnerie Supersuite, Curnamona Province, South Australia. *MESA J.* **2011**, *62*, 25–42.
81. Wade, C.E.; Reid, A.J.; Wingate, M.T.D.; Jagodzinski, E.A.; Barovich, K. Geochemistry and geochronology of the c. 1585Ma Benagerie Volcanic Suite, southern Australia: Relationship to the Gawler Range Volcanics and implications for the petrogenesis of a Mesoproterozoic silicic large igneous province. *Precambrian Res.* **2012**, *206–207*, 17–35. [CrossRef]
82. Kromkhun, K.; Foden, J.D.; Hore, S.B.; Baines, G. Geochronology and Hf isotopes of the bimodal mafic–felsic high heat producing igneous suite from Mt Painter Province, South Australia. *Gondwana Res.* **2013**, *24*, 1067–1079. [CrossRef]
83. Reid, A.J.; Jagodzinski, E.A.; Fraser, G.L.; Pawley, M.J. SHRIMP U–Pb zircon age constraints on the tectonics of the Neoarchean to early Paleoproterozoic transition within the Mulgathing Complex, Gawler Craton, South Australia. *Precambrian Res.* **2014**, *250*, 27–49. [CrossRef]
84. Reid, A.J.; Payne, J.L. Magmatic zircon Lu–Hf isotopic record of juvenile addition and crustal reworking in the Gawler Craton, Australia. *Lithos* **2017**, *292–293*, 294–306. [CrossRef]
85. Williams, M.A.; Reid, A.J. Linking lithostratigraphy to mineral potential for the Archean to earliest Paleoproterozoic Mulgathing Complex, central Gawler Craton. *MESA J.* **2021**, *94*, 4–18.

86. Smithies, R.H.; Howard, H.M.; Evins, P.M.; Kirkland, C.L.; Bodorkos, S.; Wingate, M.T.D. *The West Musgrave Complex-New Geological Insights from Recent Mapping, Geochronology, and Geochemical Studies*; Record 2008/19; Geological Survey of Western Australia: Perth, Australia, 2008.
87. Smithies, R.H.; Howard, H.M.; Evins, P.M.; Kirkland, C.L.; Kelsey, D.E.; Hand, M.; Wingate, M.T.D.; Collins, A.S.; Belousova, E.A. High-Temperature Granite Magmatism, Crust–Mantle Interaction and the Mesoproterozoic Intracontinental Evolution of the Musgrave Province, Central Australia. *J. Petrol.* **2011**, *52*, 931–958. [CrossRef]
88. Wade, B.P.; Kelsey, D.E.; Hand, M.; Barovich, K.M. The Musgrave Province: Stitching north, west and south Australia. *Precambrian Res.* **2008**, *166*, 370–386. [CrossRef]
89. Smits, R.G.; Collins, W.J.; Hand, M.; Dutch, R.; Payne, J. A Proterozoic Wilson cycle identified by Hf isotopes in central Australia: Implications for the assembly of Proterozoic Australia and Rodinia. *Geology* **2014**, *42*, 231–234. [CrossRef]
90. Howard, H.M.; Smithies, R.H.; Kirkland, C.L.; Kelsey, D.E.; Aitken, A.; Wingate, M.T.D.; Quentin de Gromard, R.; Spaggiari, C.V.; Maier, W.D. The burning heart—The Proterozoic geology and geological evolution of the west Musgrave Region, central Australia. *Gondwana Res.* **2015**, *27*, 64–94. [CrossRef]
91. Korsch, R.J.; Huston, D.L.; Henderson, R.A.; Blewett, R.S.; Withnall, I.W.; Fergusson, C.L.; Collins, W.J.; Saygin, E.; Kositcin, N.; Meixner, A.J.; et al. Crustal architecture and geodynamics of North Queensland, Australia: Insights from deep seismic reflection profiling. *Tectonophysics* **2012**, *572–573*, 76–99. [CrossRef]
92. Fergusson, C.L.; Henderson, R.A.; Fanning, C.M.; Withnall, I.W. Detrital zircon ages in Neoproterozoic to Ordovician siliciclastic rocks, northeastern Australia: Implications for the tectonic history of the East Gondwana continental margin. *J. Geol. Soc.* **2007**, *164*, 215–225. [CrossRef]
93. Wysoczanski, R.J.; Allibone, A.H. Age, Correlation, and Provenance of the Neoproterozoic Skelton Group, Antarctica: Grenville Age Detritus on the Margin of East Antarctica. *J. Geol.* **2004**, *112*, 401–416. [CrossRef]
94. Page, R.W.; Conor, C.H.H.; Stevens, B.P.J.; Gibson, G.M.; Preiss, W.V.; Southgate, P.N. Correlation of Olary and Broken Hill Domains, Curnamona Province: Possible Relationship to Mount Isa and Other North Australian Pb-Zn-Ag-Bearing Successions. *Econ. Geol.* **2005**, *100*, 663–676. [CrossRef]
95. Conor, C.H.H.; Preiss, W.V. Understanding the 1720–1640Ma Palaeoproterozoic Willyama Supergroup, Curnamona Province, Southeastern Australia: Implications for tectonics, basin evolution and ore genesis. *Precambrian Res.* **2008**, *166*, 297–317. [CrossRef]
96. Payne, J.L.; Barovich, K.M.; Hand, M. Provenance of metasedimentary rocks in the northern Gawler Craton, Australia: Implications for Palaeoproterozoic reconstructions. *Precambrian Res.* **2006**, *148*, 275–291. [CrossRef]
97. Barovich, K.M.; Hand, M. Tectonic setting and provenance of the Paleoproterozoic Willyama Supergroup, Curnamona Province, Australia: Geochemical and Nd isotopic constraints on contrasting source terrain components. *Precambrian Res.* **2008**, *166*, 318–337. [CrossRef]
98. McAvaney, S. The Cooyerdoo Granite: Paleo- and Mesoarchean basement of the Gawler Craton. *MESA J.* **2012**, *65*, 31–40.
99. Close, D.F. Chapter 21: Musgrave Province. In *Geology and Mineral Resources of the Northern Territory*; Special Publication 5; Ahmad, M., Munson, T.J., Eds.; Northern Territory Geological Survey: Darwin, Australia, 2013.
100. Hand, M.; Reid, A.; Jagodzinski, L. Tectonic Framework and Evolution of the Gawler Craton, Southern Australia. *Econ. Geol.* **2007**, *102*, 1377–1395. [CrossRef]
101. Morrissey, L.J.; Barovich, K.M.; Hand, M.; Howard, K.E.; Payne, J.L. Magmatism and metamorphism at ca. 1.45 Ga in the northern Gawler Craton: The Australian record of rifting within Nuna (Columbia). *Geosci. Front.* **2019**, *10*, 175–194. [CrossRef]
102. Payne, J.L.; Ferris, G.; Barovich, K.M.; Hand, M. Pitfalls of classifying ancient magmatic suites with tectonic discrimination diagrams: An example from the Paleoproterozoic Tunkillia Suite, southern Australia. *Precambrian Res.* **2010**, *177*, 227–240. [CrossRef]
103. Walter, M.R.; Veevers, J.J.; Calver, C.R.; Grey, K. Neoproterozoic stratigraphy of the Centralian Superbasin, Australia. *Precambrian Res.* **1995**, *73*, 173–195. [CrossRef]
104. Munson, T.J.; Kruse, P.D.; Ahmad, M. Chapter 22: Centralian Superbasin. In *Geology and Mineral Resources of the Northern Territory*; Special Publication 5; Ahmad, M., Munson, T.J., Eds.; Northern Territory Geological Survey: Darwin, Australia, 2013.
105. Normington, V.J.; Donnellan, N.C. *Characterisation of the Neoproterozoic Succession of the Northeastern Amadeus Basin, Northern Territory*; Record 2020-010; Northern Territory Geological Survey: Darwin, Australia, 2020.
106. Haines, P.W.; Allen, H.J. *Geological Reconnaissance of the Southern Murraba Basin, Western Australia: Revised Stratigraphic Position within the Centralian Superbasin and Hydrocarbon Potential*; Record 2017/4; Geological Survey of Western Australia: Perth, Australia, 2017.
107. Normington, V.J.; Edgoose, C.J. Neoproterozoic stratigraphic revisions to key drillholes in the Amadeus Basin—implications for basin palaeogeography and petroleum and minerals potential. In Proceedings of the AGES 2018, Alice Springs, Australia, 20–21 March 2018.
108. Maidment, D.W.; Williams, I.S.; Hand, M. Testing long-term patterns of basin sedimentation by detrital zircon geochronology, Centralian Superbasin, Australia. *Basin Res.* **2007**, *19*, 335–360. [CrossRef]
109. Al-Kiyumi, M. Constraining the Age and Provenance of the Basal Quartzites of the Centralian Superbasin. Ph.D. Thesis, University of Adelaide, Adelaide, Australia, 2018.
110. Fernandes, C.M.; Duffles Teixeira, P.A.; Mendes, J.C. Constraining crystallization conditions during the Cambro-Ordovician post-collisional magmatism at Araçuaí belt (SE Brazil): Zircon as key petrologic witness. *J. S. Am. Earth. Sci.* **2021**, *108*, 103235. [CrossRef]

111. Grimes, C.B.; John, B.E.; Cheadle, M.J.; Mazdab, F.K.; Wooden, J.L.; Swapp, S.; Schwartz, J.J. On the occurrence, trace element geochemistry, and crystallization history of zircon from in situ ocean lithosphere. *Contrib. Mineral. Petrol.* **2009**, *158*, 757–783. [CrossRef]
112. Grimes, C.B.; John, B.E.; Kelemen, P.B.; Mazdab, F.K.; Wooden, J.L.; Cheadle, M.J.; Hanghøj, K.; Schwartz, J.J. Trace element chemistry of zircons from oceanic crust: A method for distinguishing detrital zircon provenance. *Geology* **2007**, *35*, 643–646. [CrossRef]
113. Grimes, C.B.; Wooden, J.L.; Cheadle, M.J.; John, B.E. "Fingerprinting" tectono-magmatic provenance using trace elements in igneous zircon. *Contrib. Mineral. Petrol.* **2015**, *170*, 46. [CrossRef]
114. Hawkesworth, C.J.; Kemp, A.I.S. Using hafnium and oxygen isotopes in zircons to unravel the record of crustal evolution. *Chem. Geol.* **2006**, *226*, 144–162. [CrossRef]
115. Campbell, M.J.; Rosenbaum, G.; Allen, C.M.; Spandler, C. Continental crustal growth processes revealed by detrital zircon petrochronology: Insights from Zealandia. *J. Geophys. Res. Solid Earth* **2020**, *125*, e2019JB019075. [CrossRef]
116. Hoskin, P.W.O.; Ireland, T.R. Rare earth element chemistry of zircon and its use as a provenance indicator. *Geology* **2000**, *28*, 627–630. [CrossRef]
117. Hoskin, P.W.O.; Schaltegger, U. The composition of zircon and igneous and metamorphic petrogenesis. *Rev. Mineral. Geochem.* **2003**, *53*, 27–62. [CrossRef]
118. Rubatto, D. Zircon trace element geochemistry: Partitioning with garnet and the link between U–Pb ages and metamorphism. *Chem. Geol.* **2002**, *184*, 123–138. [CrossRef]
119. Collins, A.S.; Reddy, S.M.; Buchan, C.; Mruma, A. Temporal constraints on Palaeoproterozoic eclogite formation and exhumation (Usagaran Orogen, Tanzania). *Earth Planet. Sci. Lett.* **2004**, *224*, 175–192. [CrossRef]
120. Anenburg, M.; Williams, M.J. Quantifying the Tetrad Effect, Shape Components, and Ce–Eu–Gd Anomalies in Rare Earth Element Patterns. *Math. Geosci.* **2021**, *54*, 47–70. [CrossRef]
121. Li, Z.-X.; Powell, C.M. An outline of the palaeogeographic evolution of the Australasian region since the beginning of the Neoproterozoic. *Earth-Sci. Rev.* **2001**, *53*, 237–277. [CrossRef]
122. Wang, P.; Zhao, G.; Liu, Q.; Han, Y.; Yao, J.; Li, J. Zircons from the Tarim basement provide insights into its positions in Columbia and Rodinia supercontinents. *Precambrian Res.* **2020**, *341*, 105621. [CrossRef]
123. Cawood, P.A.; Wang, W.; Zhao, T.; Xu, Y.; Mulder, J.A.; Pisarevsky, S.A.; Zhang, L.; Gan, C.; He, H.; Liu, H.; et al. Deconstructing South China and consequences for reconstructing Nuna and Rodinia. *Earth-Sci. Rev.* **2020**, *204*, 103169. [CrossRef]
124. Cawood, P.A.; Zhao, G.; Yao, J.; Wang, W.; Xu, Y.; Wang, Y. Reconstructing South China in Phanerozoic and Precambrian supercontinents. *Earth-Sci. Rev.* **2018**, *186*, 173–194. [CrossRef]
125. Hui, B.; Dong, Y.; Zhang, F.; Sun, S.; He, S. Neoproterozoic active margin in the northwestern Yangtze Block, South China: New clues from detrital zircon U–Pb geochronology and geochemistry of sedimentary rocks from the Hengdan Group. *Geol. Mag.* **2021**, *158*, 842–858. [CrossRef]
126. Wu, G.; Yang, S.; Liu, W.; Nance, R.D.; Chen, X.; Wang, Z.; Xiao, Y. Switching from advancing to retreating subduction in the Neoproterozoic Tarim Craton, NW China: Implications for Rodinia breakup. *Geosci. Front.* **2021**, *12*, 161–171. [CrossRef]
127. Merdith, A.S.; Collins, A.S.; Williams, S.E.; Pisarevsky, S.A.; Foden, J.D.; Archibald, D.B.; Blades, M.L.; Alessio, B.L.; Armistead, S.E.; Plavsa, D.; et al. A full-plate global reconstruction of the Neoproterozoic. *Gondwana Res.* **2017**, *50*, 84–134. [CrossRef]
128. Park, Y.; Swanson-Hysell, N.L.; Xian, H.; Zhang, S.; Condon, D.J.; Fu, H.; Macdonald, F.A. A Consistently High-Latitude South China From 820 to 780 Ma: Implications for Exclusion from Rodinia and the Feasibility of Large-Scale True Polar Wander. *J. Geophys. Res. Solid Earth* **2021**, *126*, e2020JB021541. [CrossRef]
129. Cawood, P.A.; Wang, Y.; Xu, Y.; Zhao, G. Locating South China in Rodinia and Gondwana: A fragment of greater India lithosphere? *Geology* **2013**, *41*, 903–906. [CrossRef]
130. Korsch, R.J.; Kositcin, N. *South Australian Seismic and MT Workshop 2010*; Record 2010/10; Geoscience Australia: Canberra, Australian, 2010.
131. Keranen, K.; Klemperer, S.L. Discontinuous and diachronous evolution of the Main Ethiopian Rift: Implications for development of continental rifts. *Earth Planet. Sci. Lett.* **2008**, *265*, 96–111. [CrossRef]
132. Corti, G. Continental rift evolution: From rift initiation to incipient break-up in the Main Ethiopian Rift, East Africa. *Earth-Sci. Rev.* **2009**, *96*, 1–53. [CrossRef]
133. Williams, F.M. *Understanding Ethiopia: Geology and Scenery*, 1st ed.; Springer: Cham, Switzerland, 2016.
134. Purcell, P.G. Re-imagining and re-imaging the development of the East African Rift. *Pet. Geosci.* **2018**, *24*, 21–40. [CrossRef]
135. Varet, J. *Geology of Afar (East Africa)*, 1st ed.; Springer: Cham, Switzerland, 2018.
136. Zwaan, F.; Corti, G.; Keir, D.; Sani, F. A review of tectonic models for the rifted margin of Afar: Implications for continental break-up and passive margin formation. *J. Afr. Earth Sci.* **2020**, *164*, 103649. [CrossRef]
137. Boone, S.C.; Balestrieri, M.-L.; Kohn, B. Tectono-Thermal Evolution of the Red Sea Rift. *Front. Earth Sci.* **2021**, *9*, 588. [CrossRef]
138. Stein, S.; Stein, C.A.; Elling, R.; Kley, J.; Keller, G.R.; Wysession, M.; Rooney, T.; Frederiksen, A.; Moucha, R. Insights from North America's failed Midcontinent Rift into the evolution of continental rifts and passive continental margins. *Tectonophysics* **2018**, *744*, 403–421. [CrossRef]

139. Allen, D.J.; Braile, L.W.; Hinze, W.J.; Mariano, J. Chapter 10 The midcontinent rift system, U.S.A.: A major proterozoic continental rift. In *Developments in Geotectonics*; Olsen, K.H., Ed.; Elsevier: Amsterdam, The Netherlands, 2006; Volume 25, pp. 375–407, XVI–XIX.
140. Meaney, K.J. Proterozoic crustal growth in the southeastern Gawler Craton: The development of the Barossa Complex, and an assessment of the detrital zircon method. Doctoral Thesis, University of Adelaide, Adelaide, South Australia, 2017.
141. Morrissey, L.J.; Hand, M.; Wade, B.P.; Szpunar, M.A. Early Mesoproterozoic metamorphism in the Barossa Complex, South Australia: Links with the eastern margin of Proterozoic Australia. *Aust. J. Earth Sci.* **2013**, *60*, 769–795. [CrossRef]
142. Nordsvan, A.R.; Collins, W.J.; Li, Z.-X.; Spencer, C.J.; Pourteau, A.; Withnall, I.W.; Betts, P.G.; Volante, S. Laurentian crust in northeast Australia: Implications for the assembly of the supercontinent Nuna. *Geology* **2018**, *46*, 251–254. [CrossRef]
143. Rutherford, L.; Hand, M.; Barovich, K. Timing of Proterozoic metamorphism in the southern Curnamona Province: Implications for tectonic models and continental reconstructions. *Aust. J. Earth Sci.* **2007**, *54*, 65–81. [CrossRef]
144. Tiddy, C.J.; Giles, D. Suprasubduction zone model for metal endowment at 1.60–1.57 Ga in eastern Australia. *Ore Geol. Rev.* **2020**, *122*, 103483. [CrossRef]
145. Volante, S.; Pourteau, A.; Collins, W.J.; Blereau, E.; Li, Z.X.; Smit, M.; Evans, N.J.; Nordsvan, A.R.; Spencer, C.J.; McDonald, B.J.; et al. Multiple P–T–d–t paths reveal the evolution of the final Nuna assembly in northeast Australia. *J. Metamorph. Geol.* **2020**, *38*, 593–627. [CrossRef]
146. Hill, R.I.; Campbell, I.H.; Davies, G.F.; Griffiths, R.W. Mantle Plumes and Continental Tectonics. *Science* **1992**, *256*, 186. [CrossRef] [PubMed]
147. Armit, R.J.; Betts, P.G.; Schaefer, B.F.; Ailleres, L. Constraints on long-lived Mesoproterozoic and Palaeozoic deformational events and crustal architecture in the northern Mount Painter Province, Australia. *Gondwana Res.* **2012**, *22*, 207–226. [CrossRef]
148. Paul, E.; Flöttmann, T.; Sandiford, M. Structural geometry and controls on basement-involved deformation in the northern Flinders Ranges, Adelaide Fold Belt, South Australia. *Aust. J. Earth Sci.* **1999**, *46*, 343–354. [CrossRef]
149. Barovich, K.M.; Foden, J. A Neoproterozoic flood basalt province in southern-central Australia: Geochemical and Nd isotope evidence from basin fill. *Precambrian Res.* **2000**, *100*, 213–234. [CrossRef]
150. Fanning, C.M.; Ludwig, K.R.; Forbes, B.G.; Preiss, W.V. Single and multiple grain U–Pb zircon analyses for the early Adelaidean Rook Tuff, Willouran Ranges, South Australia. In *Eighth Australian Geological Convention: "Earth Resources in Space and Time"*; Abstracts 10; Geological Society of Australia: Sydney, Australia, 1986; pp. 71–72.
151. Armistead, S.E.; Collins, A.S.; Buckman, S.; Atkins, R. Age and geochemistry of the Boucaut Volcanics in the Neoproterozoic Adelaide Rift Complex, South Australia. *Aust. J. Earth Sci.* **2020**, *68*, 580–589. [CrossRef]
152. Preiss, W.V.; Drexel, J.F.; Reid, A.J. Definition and age of the Kooringa Member of the Skillogalee Dolomite: Host for Neoproterozoic (c. 790 Ma) porphyry related copper mineralisation at Burra. *MESA J.* **2009**, *55*, 19–33.
153. Von der Borch, C.C. Evolution of late proterozoic to early paleozoic Adelaide foldbelt, Australia: Comparisons with postpermian rifts and passive margins. *Tectonophysics* **1980**, *70*, 115–134. [CrossRef]
154. Zhao, J.-x.; McCulloch, M.T.; Korsch, R.J. Characterisation of a plume-related~800 Ma magmatic event and its implications for basin formation in central-southern Australia. *Earth Planet. Sci. Lett.* **1994**, *121*, 349–367. [CrossRef]
155. McKenzie, D.P.; Davies, D.; Molnar, P. Plate Tectonics of the Red Sea and East Africa. *Nature* **1970**, *226*, 243–248. [CrossRef] [PubMed]
156. Tesfaye, S.; Harding, D.J.; Kusky, T.M. Early continental breakup boundary and migration of the Afar triple junction, Ethiopia. *GSA Bull.* **2003**, *115*, 1053–1067. [CrossRef]
157. Barberi, F.; Tazieff, H.; Varet, J. Volcanism in the Afar depression: Its tectonic and magmatic significance. *Tectonophysics* **1972**, *15*, 19–29. [CrossRef]
158. Lloyd, J.; Collins, A.; Blades, M.; Gilbert, S.; Amos, K. LA-ICP-MS detrital zircon standards results. *Figshare* **2022**. [CrossRef]
159. Lloyd, J.; Collins, A.; Blades, M.; Amos, K.; Gilbert, S. Callanna Group detrital zircon dataset (Lloyd et al.). *Figshare* **2022**. [CrossRef]
160. Kuhn, B.K.; Birbaum, K.; Luo, Y.; Günther, D. Fundamental studies on the ablation behaviour of Pb/U in NIST 610 and zircon 91500 using laser ablation inductively coupled plasma mass spectrometry with respect to geochronology. *J. Anal. At. Spectrom.* **2010**, *25*, 21–27. [CrossRef]
161. Thompson, J.M.; Meffre, S.; Danyushevsky, L. Impact of air, laser pulse width and fluence on U–Pb dating of zircons by LA-ICPMS. *J. Anal. At. Spectrom.* **2018**, *33*, 221–230. [CrossRef]
162. Allen, C.M.; Campbell, I.H. Identification and elimination of a matrix-induced systematic error in LA–ICP–MS 206Pb/238U dating of zircon. *Chem. Geol.* **2012**, *332–333*, 157–165. [CrossRef]
163. Miliszkiewicz, N.; Walas, S.; Tobiasz, A. Current approaches to calibration of LA-ICP-MS analysis. *J. Anal. At. Spectrom.* **2015**, *30*, 327–338. [CrossRef]
164. Marillo-Sialer, E.; Woodhead, J.; Hergt, J.; Greig, A.; Guillong, M.; Gleadow, A.; Evans, N.; Paton, C. The zircon 'matrix effect': Evidence for an ablation rate control on the accuracy of U–Pb age determinations by LA-ICP-MS. *J. Anal. At. Spectrom.* **2014**, *29*, 981–989. [CrossRef]
165. Košler, J.; Wiedenbeck, M.; Wirth, R.; Hovorka, J.; Sylvester, P.; Míková, J. Chemical and phase composition of particles produced by laser ablation of silicate glass and zircon—Implications for elemental fractionation during ICP-MS analysis. *J. Anal. At. Spectrom.* **2005**, *20*, 402–409. [CrossRef]

166. Schaltegger, U.; Schmitt, A.K.; Horstwood, M.S.A. U–Th–Pb zircon geochronology by ID-TIMS, SIMS, and laser ablation ICP-MS: Recipes, interpretations, and opportunities. *Chem. Geol.* **2015**, *402*, 89–110. [CrossRef]
167. Paton, C.; Woodhead, J.D.; Hellstrom, J.C.; Hergt, J.M.; Greig, A.; Maas, R. Improved laser ablation U-Pb zircon geochronology through robust downhole fractionation correction. *Geochem. Geophys. Geosyst.* **2010**, *11*. [CrossRef]
168. Ver Hoeve, T.J.; Scoates, J.S.; Wall, C.J.; Weis, D.; Amini, M. Evaluating downhole fractionation corrections in LA-ICP-MS U-Pb zircon geochronology. *Chem. Geol.* **2018**, *483*, 201–217. [CrossRef]
169. Souders, A.K.; Sylvester, P.J. Accuracy and precision of non-matrix-matched calibration for lead isotope ratio measurements of lead-poor minerals by LA-MC-ICPMS. *J. Anal. At. Spectrom.* **2010**, *25*, 975–988. [CrossRef]
170. Guillong, M.; Wotzlaw, J.-F.; Looser, N.; Laurent, O. Evaluating the reliability of U–Pb laser ablation inductively coupled plasma mass spectrometry (LA-ICP-MS) carbonate geochronology: Matrix issues and a potential calcite validation reference material. *Geochronology* **2020**, *2*, 155–167. [CrossRef]
171. Halpin, J.A.; Jensen, T.; McGoldrick, P.; Meffre, S.; Berry, R.F.; Everard, J.L.; Calver, C.R.; Thompson, J.; Goemann, K.; Whittaker, J.M. Authigenic monazite and detrital zircon dating from the Proterozoic Rocky Cape Group, Tasmania: Links to the Belt-Purcell Supergroup, North America. *Precambrian Res.* **2014**, *250*, 50–67. [CrossRef]
172. Large, R.R.; Meffre, S.; Burnett, R.; Guy, B.; Bull, S.; Gilbert, S.E.; Goemann, K.; Danyushevsky, L.V. Evidence for an Intrabasinal Source and Multiple Concentration Processes in the Formation of the Carbon Leader Reef, Witwatersrand Supergroup, South Africa. *Econ. Geol.* **2013**, *108*. [CrossRef]
173. Standish, C.; Dhuime, B.; Chapman, R.; Coath, C.; Hawkesworth, C.; Pike, A. Solution and laser ablation MC-ICP-MS lead isotope analysis of gold. *J. Anal. At. Spectrom.* **2013**, *28*, 217–225. [CrossRef]
174. Schaltegger, U.; Ovtcharova, M.; Gaynor, S.P.; Schoene, B.; Wotzlaw, J.-F.; Davies, J.F.H.L.; Farina, F.; Greber, N.D.; Szymanowski, D.; Chelle-Michou, C. Long-term repeatability and interlaboratory reproducibility of high-precision ID-TIMS U–Pb geochronology. *J. Anal. At. Spectrom.* **2021**. [CrossRef] [PubMed]